EFFECT OF MAGNETIC ANISOTROPY AND PARTICLE SIZE DISTRIBUTION ON MAGNETIZATION OF ANTIFERROMAGNETIC NANOPARTICLES

A Thesis Submitted
in partial fulfillment of the requirements
for the degree of
Doctor of Philosophy

by
Navneet Kaur
(Regn. No. 901412005)

Under the Guidance of
Dr. S. D. Tiwari
(Associate Professor)

THAPAR INSTITUTE
OF ENGINEERING & TECHNOLOGY
(Deemed to be University)

to the
SCHOOL OF PHYSICS AND MATERIALS SCIENCE
THAPAR INSTITUTE OF ENGINEERING AND TECHNOLOGY, PATIALA 147004
INDIA
October 2020

DECLARATION

I hereby certify that work presented in this thesis entitled "*Effect of Magnetic Anisotropy and Particle Size Distribution on Magnetization of Antiferromagnetic Nanoparticles*" in partial fulfillment of the requirement of the award of degree of DOCTOR OF PHILOSOPHY in the School of Physics and Materials Science, Thapar Institute of Engineering and Technology, Patiala is an authentic record of my own work carried out under supervision of Dr. S. D. Tiwari. The matter embodied in this thesis has not been submitted in part or full to any other university or institute for the award of any degree.

Navneet Kaur

This is to certify that the above statement made by the candidate is true to the best of my knowledge.

S.D. Tiwari

Dr. S. D. Tiwari
Associate Professor
School of Physics and Materials Science
Thapar Institute of Engineering and Technology
Patiala

SYNOPSIS

Nanomaterials show interesting properties which make them appealing in various disciplines of science and engineering. Behavior of these materials is different from corresponding bulk form. Finite size and surface effects are mainly responsible for these new properties. Superparamagnetism is one such unique phenomenon. This behavior is only exhibited by sufficiently small particles of ferro, ferri and antiferromagnetic materials. Temperature and applied magnetic field strength are two well known parameters affecting the magnetization of magnetic particles. But, there are also several other factors affecting the magnetization process in these systems. Effect of particle size distribution and magnetic anisotropy on the magnetization process of two antiferromagnetic nanoparticle systems have been discussed in this work. An outline of the thesis is as follows.

Chapter 1 contains introduction of the work. It begins with physics of magnetic materials followed by the change in behavior of materials with reduction in size, properties of nanoparticles, magnetism of nanoparticles, magnetization process in nanoparticles, literature review and motivation.

Chapter 2 describes processing of Ferritin and synthesis of two samples of NiO nanopar-

ticles. It also contains working principles of x-ray diffractometer, transmission electron microscope, thermogravimetric analyzer, atomic absorption spectrometer and vibrating sample magnetometer.

Chapter 3 describes the detailed characterization results on ferritin. Structural and morphological characterization of ferritin is done by using x-ray diffractometer and transmission electron microscope. Ferritin particles are found to be poorly crystalline. It has a core-shell structure. The obtained transmission electron microscope shows the dense cores only. Average core size is found to be about 8 nm. Thermal stability of ferritin is analyzed using thermogravimetric analyzer. The core of ferritin is supposed to contain ferrihydrite. Therefore, the thermal behavior of ferritin is expected to be similar to ferrihydrite. But, the thermal decomposition of ferritin is found to be different than that of ferrihydrite. It indicates that the ferritin core consists of some other phases along with ferrihydrite. Zero field cooled and field cooled susceptibility as a function of temperature are measured in an applied field of 250 G. Both curves are seen to bifurcate at 17 K. The M-B loop at 5 K shows a hysteresis. But, the M-B loop at 300 K does not show any hysteresis. These measurements confirm that the behavior of ferritin is superparamagnetic. Magnetization of ferritin is also measured as a function of applied magnetic field at different temperatures in superparamagnetic region. These curves are fitted to suitable expressions to study the effect of particle size distribution and magnetic anisotropy following a non-linear least square fit procedure. It is found that both parameters affect the magnetization process of

ferritin.

Chapter 4 describes characterization of two samples of NiO nanoparticles prepared by thermal decomposition of nickel hydroxide. Structural characterization of the synthesized nickel hydroxide powder is done using x-ray diffractometer. Thermogravimetric analysis of nickel hydroxide shows that this material decomposes to NiO on heating above 250 ^{o}C. Two samples of NiO nanoparticles are prepared by heating nickel hydroxide powder at 250 and 300 ^{o}C in an inert atmosphere. The structural and morphological characterizations of these particles are done by x-ray diffractometer and transmission electron microscope. Both samples have wide particle size distributions. Average particle sizes are found to be 5 and 8 nm. Zero field cooled and field cooled susceptibility as a function of temperature curves in an external magnetic field of 250 G are seen to bifurcate at 300 and 330 K. The M-B loops at 10 K have hysteresis. But the M-B loops at 350 K do not have any hysteresis. These observations indicate that both samples of NiO nanoparticles are superparamagnetic. Magnetization as a function of applied magnetic field data at 350 K are fitted to a suitable expression which considers the role of particle size distribution. This analysis is found to be useful in estimating particle size distribution. The estimated particle size distributions for both samples are compared with corresponding distributions determined from transmission electron micrographs.

Chapter 5 summarizes the carried out work. It also discusses scope for future work.

ACKNOWLEDGEMENTS

It is my privilege to owe my gratitude to all those who have been with me during my thesis work. I am grateful to the Almighty for giving me strength to face the hardships in life. Thank you, Waheguru.

First and foremost, I want to sincerely thank my thesis supervisor, Dr. S. D. Tiwari, for his profound support, guidance, suggestions, and encouragement throughout the course of this work. He constantly helped me in solving problems and aspired me to be successful. This work would not have been possible without his moral support. Also, I would like to extend my special thanks to my research committee members, Dr. B. C. Mohanty, Dr. Puneet Sharma, and Dr. A. K. Lal for their encouragement, support, and insightful comments. Additionally, I would like to express my gratitude towards Dr. Rafat Siddique (Dean of Research and Sponsored Projects), Dr. O. P. Pandey (Head of the SPMS) and Dr. Kulvir Singh (Associate Dean of Research and Sponsored Projects) for their support and extensive help throughout this course. I thank Dr. B. N. Chudasama for thermal characterization of my samples.

I would like to thank my parents, Dr. Parmeshwar Singh and Mrs. Manjit Kaur, for their love and support throughout my life, as it wouldnt have been possible without them. They always encouraged me to sort out the challenging situations calmly, which helped me to become a better person in every aspect of the life. I am forever indebted to my parents for giving me the opportunities and experiences that have made me who I am. I want to express my wholehearted thank to my brother, Mr. Gurparkash Singh, for his emotional support, unwavering faith, and guidance throughout my career.

I would like to express my deepest appreciation to my friends Miss Shobhneek Kaur and Mrs. Nisha Gill for their cordial help, moral support, and the valuable discussions during the thesis work. Also, a special thanks goes to Mrs. Meenu, Miss Ridhi Tomar, Miss Shilpy Sharma and Mrs. Garima from whom I have learnt the art of happiness and never give up approach.

Finally, I would like to acknowledge the staff members of SAI Lab for their technical help and cooperation.

Navneet Kaur

Dedicated to My Parents

PUBLICATIONS

In SCI Journals

1. *Role of particle size distribution and magnetic anisotropy on magnetization of antiferromagetic nanoparticles.*
   Navneet Kaur and S. D. Tiwari, J. Phys. Chem. Solids **123**, 279 (2018).

2. *Thermal decomposition of ferritin core.*
   Navneet Kaur and S. D. Tiwari, Appl. Phys. A **125**, 805 (2019).

3. *Role of wide particle size distribution on magnetization.*
   Navneet Kaur and S. D. Tiwari, Appl. Phys. A **126**, 349 (2020).

In Conferences

1. *Estimation of Magnetic Anisotropy Constant of Magnetic Nanoparticles.*
   Navneet Kaur and S. D. Tiwari, 64^{th} DAE Solid State Physics Symposium (DAE-SSPS 2019) held at IIT Jodhpur, India during December 18-22, 2019.

2. *Superparamagnetic Behavior of NiO Nanoparticles.*
   Navneet Kaur and S. D. Tiwari, 10^{th} International Conference on Materials and Advance Technology (ICMAT 2019), held at Marina Bay Sands, Singapore during June 23-28, 2019.

3. *Size Dependence of Magnetic Anisotropy Constant in Antiferromagnetic Nanoparticle System.*
   Navneet Kaur and S. D. Tiwari, International Conference on Advanced Materials (ICAM 2017) held at Nirmalgiri College, Kerala, India during June 12-14, 2019.

4. *Thermal and Magnetization Characterization of Ferritin.*
   Navneet Kaur and S. D. Tiwari, 6^{th} Global Nanotechnology Congress and Expo (GNCE 2019) held in Dubai, UAE during April 15-16, 2019.

5. *Influence of magnetic Anisotropy on Magnetization of Magnetic Nanoparticles.*
   Navneet Kaur and S. D. Tiwari, 2^{nd} International Conference on Condensed Matter and Applied Physics (ICC 2017) held at Govt. Engineering College, Bikaner, India during Nov. 24-25, 2017.

6. *Magnetic Properties of Iron Storage Protein Ferritin.*
   Navneet Kaur and S. D. Tiwari, International Conference on Nanotechnology (ICN 2017) held at IIT Roorkee, Uttarakhand, India during Dec. 06-08, 2017.

7. *Superparamagnetic Behaviour of Iron Storage Protein Ferritin.*
   Navneet Kaur and S. D. Tiwari, International Conference on Nanoscience and Nanotechnology (ICONN 2017) held at SRM University, Chennai, India during August 09-11, 2017.

PARTICIPATION IN WORKSHOP AND SCHOOLS

1. MRS-Singapore Summer School on Magnetic and Spintronic Materials held at Nanyang Technical University, Singapore during June 20-22, 2019.

2. Summer school on magnetism held at Thapar Institute of Engineering and Technology, Patiala, India during July 11-15, 2016.

3. National Workshop on Advanced Technique for Surface Characterization (NWATSC 2015) held at Thapar Institute of Engineering and Technology, Patiala, India during Oct. 28-30, 2015.

CONTENTS

Synopsis . . . iii

Acknowledgements . . . vi

Publications . . . ix

Publications . . . xi

List of Figures . . . xiv

List of Tables . . . xvi

List of Abbreviations . . . xvii

List of Notations . . . xviii

1. Introduction . . . 1
- 1.1 Physics of Magnetic Materials . . . 2
  - 1.1.1 Classical Langevin theory . . . 4
- 1.2 Nanoparticles . . . 5
- 1.3 Properties of Nanoparticles . . . 6
  - 1.3.1 Physical properties . . . 6
  - 1.3.2 Optical properties . . . 7
  - 1.3.3 Chemical properties . . . 7
  - 1.3.4 Electronic properties . . . 8
  - 1.3.5 Mechanical properties . . . 8
  - 1.3.6 Magnetic properties . . . 9
- 1.4 Magnetocrystalline Anisotropy . . . 9
- 1.5 Superparamagnetism . . . 12
  - 1.5.1 Behaviour of superparamagnetic particles . . . 14
  - 1.5.2 Applications of magnetic nanoparticles . . . 20
- 1.6 Literature Review and Motivation . . . 21

2. Experimental Details . . . 25
- 2.1 Sample Preparation . . . 25
- 2.2 Experimental Techniques . . . 26
  - 2.2.1 X-ray diffractometer . . . 26
  - 2.2.2 Thermogravimetric analyzer . . . 28

2.2.3 Transmission electron microscope 29
2.2.4 Atomic absorption spectrometer 31
2.2.5 Vibrating sample magnetometer 32

3. Ferritin Nanoparticles 34
3.1 Structural Characterization 34
3.2 Magnetization 41
3.2.1 Temperature dependence 41
3.2.2 Field dependence 42
3.3 Particle Size Distribution 43
3.4 Magnetic Anisotropy 46
3.5 Conclusion 52

4. Nickel Oxide Nanoparticles 53
4.1 Structural Characterization 53
4.2 Magnetization 57
4.2.1 Temperature dependence 57
4.2.2 Field dependence 57
4.3 Particle Size Distribution 58
4.4 Conclusion 64

5. Conclusions 65

Bibliography 68

LIST OF FIGURES

1.1 Easy axis of a hexagonal unit cell. 11
1.2 Magnetocrystalline anisotropy energy E_{an} as a function of angle β for an uniaxial system. 12
1.3 Antiferromagnetic ordering of magnetic moments (a) in one-dimensonal system with zero net magnetic moment, (b) system shows magnetic moment due to incomplete cancellation of spins, (c) in two dimensional sytem with zero net magnetic moment, and (d) one layer of spins is missing showing net magnetic moment. 14
1.4 Zero field cooled (ZFC) and field cooled (FC) susceptibility curves for superparamagnetic system. 17
1.5 Magnetization M as a function of applied magnetic field B for superparamagnetic system. 18

2.1 X-ray diffraction from parallel atomic planes. 27
2.2 Schematic representation of thermogravimetric analyzer. 29
2.3 Electron diffraction pattern from randomly oriented crystals. 30
2.4 Block diagram of atomic absorption spectrometer. 32
2.5 Arrangement of electromagnets, pickup coils, vibration unit and output unit in vibrating sample magnetometer. 33

3.1 (a) Room temperature x-ray diffraction pattern, (b) transmission electron micrograph, (c) selected area electron diffraction pattern and (d) a histogram of the distribution of particle size for ferritin. Bragg's reflections from ferritin are not detected. Dotted circles are visual guides. Indexed peaks and rings correspond to NaCl. 35
3.2 (a) TGA and (b) DTG curves for ferritin. 36
3.3 X-ray diffraction patterns of ferritin samples heated at (a) 550 and (b) 1050 ^{o}C. 37
3.4 (a) Transmission electron micrograph and (b) selected area electron diffraction pattern for ferritin sample heated at 550 ^{o}C. Dotted circles are visual guides. 38
3.5 (a) Transmission electron micrograph and (b) selected area electron diffraction pattern for ferritin sample heated at 1050 ^{o}C. Dotted circles are visual guides. 39
3.6 ZFC (solid symbol) and FC (open symbol) susceptibility χ as a function of temperature T for ferritin in 250 G applied magnetic field. 41
3.7 M-B loops for ferritin at 5 and 300 K. 42

3.8 Magnetization M as a function of applied magnetic field B for ferritin at different temperatures. 43
3.9 Magnetization M as a function of applied magnetic field B for ferritin at different temperatures. Solid lines show fit to Eq. (3.3). Inset shows histogram for particle size distribution. Curves show estimated particle size distribution. 44
3.10 Angles α, β, λ and ϕ used in calculation of magnetization. 46
3.11 (a) Log-normal distribution in particle diameter for two different values of parameters s and n and (b) calculated magnetization curves for corresponding particle size distributions considering absence (solid symbols) and presence (open symbol) of magnetic anisotropy at 250 K. 48
3.12 Magnetization M as a function of applied magnetic field B for ferritin at different temperatures. Solid lines show fit to Eq. (3.11). Inset shows histogram for particle size distribution. Curves show estimated particle size distribution. 49

4.1 X-ray diffraction pattern of β-$Ni(OH)_2$ powder sample. 53
4.2 (a) TGA and (b) DTG curves for β-$Ni(OH)_2$. 54
4.3 (a) Room temperature x-ray diffraction pattern, (b) transmission electron micrograph, (c) selected area electron diffraction pattern and (d) a histogram of the distribution of particle sizes for NiO sample prepared by heating β-$Ni(OH)_2$ at 250 ^{o}C. 55
4.4 (a) Room temperature x-ray diffraction pattern, (b) transmission electron micrograph, (c) selected area electron diffraction pattern and (d) a histogram of the distribution of particle sizes for NiO sample prepared by heating β-$Ni(OH)_2$ at 300 ^{o}C. 56
4.5 ZFC (solid symbol) and FC (open symbol) susceptibility χ as a function of temperature T for 5 and 8 nm NiO particles in 250 G applied magnetic field. 58
4.6 M-B loops for 5 and 8 nm NiO particles at two different temperatures. 59
4.7 Magnetization M as a function of applied magnetic field B curves for 5 and 8 nm NiO particles at 350 K. 60
4.8 Magnetization M as a function of applied magnetic field B curves for 5 and 8 nm NiO particles at temperature 350 K. Solid lines shows fit to Eq. (4.2) 61
4.9 Histogram showing particle size distribution determined from transmission electron micrograph for (a) 5 and (b) 8 nm NiO particles. Solid curves show estimated particle size distribution. 62

LIST OF TABLES

3.1 Values of fit parameters N,C, s, n, and χ to Eq. (3.3) and the values of R^2 for ferritin at different temperatures. 45
3.2 Values of fit parameters N,C, K, s, n, and χ to Eq. (3.11) and the values of R^2 for ferritin at different temperatures. 50

4.1 Values of fit parameters N, s, n and χ to Eq. (4.2) for NiO samples. . . 61

LIST OF ABBREVIATIONS

XRD	X-ray diffraction
TGA	Thermogravimetric analyzer
TEM	Transmission electron microscope
VSM	Vibrating sample magnetometer
nm	nanometer
ZFC	Zero field cooled
FC	Field cooled
emu	Electromagnetic unit
g	gram
G	gauss
Oe	oestered
J	joules
m	meter
K	kelvin

LIST OF NOTATIONS

M	Magnetization
B	Magnetic induction
χ	Susceptibility
T	Temperature
T_{bf}	Bifurcation temperature
T_B	Blocking temperature
N	Number of ions per unit mass
μ	Ionic magnetic moment
k_B	Boltzmann constant
μ_B	Bohr magneton
K	Magnetic anisotropy constant
V	Particle volume
D	Particle diameter

Chapter 1

INTRODUCTION

Physics behind different states of matter has gained a privileged status in the broad field of research. Their properties give an insight into new and interesting concepts that lead to the discovery of new theories. Understanding these theories helps in bringing the development of new materials for advancements in technology. Several models were proposed to define the constituents inside matter. In ancient Greek, philosophers proposed that tiny atoms collectively build matter. At the beginning of 18^{th} century, a chemist Dalton postulated that matter is made up of indivisible small atoms. After that, many theories came into existence to shed light on the composition of matter. Later on, it was discovered that these atoms are further divisible into smaller entities. Thus, all materials are composed of the smallest fundamental block called an atom. The arrangement of atoms and the forces which bind them together is responsible for the characteristic behaviour of materials. Different states of matter have different atomic order and bonding. Certain properties, based on the bonding and arrangement of atoms, classify matters into different categories. Among these, solids are well-studied class so far. One of the most striking feature of solids is their characteristic rigidity due to the strong bonding present between their atoms. Classically, we can represent solids as an assembly of atoms connected by springs that hinder their relative motion. However, at high temperature, atoms start oscillating and displace with respect to each other. Based on the atomic arrangement, these solids can be crystalline and

non-crystalline. The most analysed class of solids is crystalline. In crystalline solids, atoms follow a regular and periodic pattern. These crystals tend to retain their long-range three-dimensional atomic arrangement which repeats in all spatial directions. Most of the solids found in nature are crystalline because this symmetry has the least configurational energy. The study of crystalline solids has become more pronounced when newer families of materials with fascinating properties have been produced. The physics of different behaviour in these solids is vast but we limit our discussion by focusing on the magnetic study of solids.

1.1 Physics of Magnetic Materials

Magnetism in crystalline solids has been known for centuries. But, this phenomenon was somewhat understood in the twentieth century. The origin of magnetism in solids was advanced by several discoveries. These discoveries were put forward to study magnetic phenomena and their effects.

The arrangement of atoms in solids is the basis for their exciting properties. Atoms contain electrons, protons and neutrons. Electrons revolve around the positively charged nucleus of an atom which holds protons and neutrons inside it. The presence of electrons in the outermost orbit affects the properties of solids. The interactions and alignment of spins in atoms decide the overall magnetic behaviour in solids. The revolving electrons around the nucleus have their respective orbits and possess orbital motion. These rotating electrons act as dipoles and contribute to the magnetic moment in crystals. The orbital magnetic moment μ_L is given by [1]

$$\mu_L = -g_L \frac{e}{2m} L, \tag{1.1}$$

where g_L is Lande splitting factor, L is orbital angular momentum, m is the mass of an electron and e is the electronic charge. The value of the Lande splitting factor is 1

for pure orbital motion. The electron also spins about its axis. Due to the orientation of these spins, the electron has a spin magnetic moment μ_S given by [1]

$$\mu_S = -g_S \frac{e}{2m} S, \tag{1.2}$$

where g_S is the Lande splitting factor and S is spin angular momentum. The value of the Lande splitting factor is 2 for a pure spin. The atomic magnetic moment has a minute contribution from the nuclear spin.

The orbiting electrons around the nucleus have their respective shells. The atoms with filled outermost shells have zero net magnetic moment. Because there is perfect cancellation of magnetic moments. But, atoms with unfilled outermost shells possess some net magnetic moment. Therefore, these unfilled outermost shells account for the magnetic moment in materials. The magnetic moments are coupled with each other via some interactions, mainly exchange, and dipolar interactions. Magnetic order in the systems is determined through the strength of these interactions and their response towards external energies.

The direct manifestation of the magnetic field is the region in space up to which magnetic forces show their influence. Crystalline solids are found to show response towards the magnetic field. Depending on their behaviour with respect to the magnetic field and the relative orientations of their magnetic moments, they are classified into diamagnetic, paramagnetic, ferromagnetic, ferrimagnetic, and antiferromagnetic materials [2–4]. Materials that show negligible response towards magnetic field are called diamagnetic. The atoms of these materials have no unpaired electron in their valence shell. So, their net magnetic moment is zero. These materials have a very low and negative value of magnetic susceptibility. Although diamagnetism is present in all materials, yet due to its weak nature it can be observed only in materials having zero atomic magnetic moment. Paramagnetic materials have unpaired electrons in their

constituent atoms. In absence of an external magnetic field, their magnetic moments are randomly oriented and cancel the effect of each other, it cause negligible magnetic moment in these materials. But, they get feebly attracted towards the externally applied magnetic field. Ferro, ferri, and antiferromagnetic materials have exchange and dipolar interactions among the magnetic moments. Due to this, these materials possess magnetic orders.

Behaviour of large magnetic crystals has been always a part of many course studies. Bulk magnetic materials have many contributions in technology as magnetic storage, sensors, electronic devices, biomedical, transportation, etc. [1, 5–9]. But, there occurs a drastic change in their properties with reduction of particle size and start exhibiting interesting phenomena [10–13].

1.1.1 Classical Langevin theory

Consider N non-interacting magnetic moments μ at temperature T. These moments will be randonly oriented which give net zero magnetization. If an external magnetic field B is applied then the moments will try to align themself along the field direction. The Zeeman energy E_z is given as

$$E_z = -\mu.B = -\mu B cos\alpha, \tag{1.3}$$

where α the angle between a magnetic moment and applied magnetic field. This energy is minimum when the particles are aligned along the magnetic field and maximum when they are antiparallel to the magnetic field. At high temperature, these moments follow Maxwell-Boltzmann statistics. The probability $f(E)$ that a moment is aligned at an angle α with the applied magnetic field is given by

$$f(E) = A\exp(\frac{-E_z}{k_B T}) = A\exp(\frac{\mu B cos\alpha}{k_B T}), \tag{1.4}$$

where A is a normalization constant. Using theory of canonical ensemble, the mean value of projection of μ along the applied magnetic field direction

$$\bar{\mu} = \frac{\int_0^\pi \mu \cos\alpha \exp(\frac{-E_z}{k_B T}) \sin\alpha d\alpha}{\int_0^\pi \exp(\frac{-E_z}{k_B T}) \sin\alpha d\alpha} = \frac{\int_0^\pi \mu \cos\alpha \exp(\frac{\mu B \cos\alpha}{k_B T}) \sin\alpha d\alpha}{\int_0^\pi \exp(\frac{\mu B \cos\alpha}{k_B T}) \sin\alpha d\alpha}. \tag{1.5}$$

Substituting $x = \frac{\mu B \cos\alpha}{k_B T}$ and solving the integrals, one gets

$$\bar{\mu} = \mu L(x), \tag{1.6}$$

where $L(x) = [\coth(x) - (\frac{1}{x})]$ is the Langevin function, $x = \frac{\mu B}{k_B T}$ and k_B is Boltzmann constant. The magnetization of the system $M(B,T) = N\bar{\mu} = N\mu L(x)$.

1.2 Nanoparticles

Particles having all three dimensions confined to nanometre range are called nanoparticles. These particles can be prepared in laboratories and also exist naturally in the environment [10, 11, 14, 15]. Their behaviour is scientifically found to be unique and engrossing [10, 13, 16]. Because of their novel behaviour, scientists are more inclined to study these particles. The study of the physics of nanoparticles is very interesting because the reduced dimensions make their behaviour significantly different than their bulk counterpart. It is due to the role of surface atoms that become prominent as the size of particle decreases. The surface to volume ratio is negligible for bulk crystals and it increases with decreasing particle size. The surface and size effects become very important once we reach the nanometer range. The engraved properties of nanoparticles are found to be promising candidates in many useful applications [17]. Novel works on the studies of nanoparticles have been reported by several authors.

The quantum size effects start dominating with reduction of particle size to nanome-

tre range [11]. It is related to the spatial confinement of electrons inside the particle. In bulk materials, the energy bands are continuous. Because the number of atoms in macro or microparticles are large and are in the order of Avogadro's number. Due to it, the atomic energy levels are closely spaced. These closely spaced energy levels overlap and form continuous energy bands. Whereas in nanoparticles, the particle size is smaller than the de Broglie wavelength associated with electrons. It restricts the motion of electrons and quantum mechanics starts playing a significant role. The confined motion of electrons is like a particle in a box and is defined by the Schrodinger equation. And therefore, the energy levels are discrete in nanoparticles. The reducing size also increases the number of surface atoms compared to the core of the particle. The increased surface energy and quantum confinement in these particles have modified the physical, optical, chemical, electronic, mechanical, and magnetic properties. Presently, the properties of these particles have brought a revolution in nanotechnology that is not recognized in any other technological development. The valuable consequences and impacts of nanoparticles on scientific advancement can only be realized if their properties are well exploited.

1.3 Properties of Nanoparticles

Size and surface effects in small particles make them own a different place from those of corresponding bulk materials. Their properties are briefly summarized below.

1.3.1 Physical properties

Reduced dimensions change the physical behaviour of materials. The increase in surface-to-volume ratio increases surface energy and decreases the cohesive energies of particles. It leads to a decrease in average interparticle strength which results in a change of thermodynamic behaviour of the system. Therefore, nanoparticles have a low melting point compared to their bulk forms. For example, the melting point of

bulk Au and GaN are 1064 and 2770 K, respectively. But, the melting points of 3 nm Au and GaN are found to be 500 and 1747 K, respectively [18]. Reduction in particle size also limits the movement of dislocations. Due to it, the hardness of nanoparticles is more than their bulk forms.

1.3.2 Optical properties

Quantum states of electrons in atomic orbitals can be varied using the light of suitable frequency. It affects the overall optical behaviour of materials. Precise knowledge of how matter and light interact to create an optical phenomenon is necessary to utilize materials in many applications. Scattering and absorption in materials can be altered by controlling the size of particles. The optical band gap in nanoparticles decreases which shifts the position of absorption peaks in materials towards lower wavelength [19]. At the nanoscale, the color of metal particles changes due to the resonance in the absorption spectrum called surface plasmon resonance [20]. In bulk materials, the plasmon frequency lies in the UV region while in nanoparticles it is in the visible region. The frequency of surface plasmon also depends upon the shape of the nanoparticle. For example, the color of gold and silicon particles becomes red at nanoscale [11].

1.3.3 Chemical properties

Chemical reactivity in nanoparticles is usually modified because the number of atoms participating in the reaction changes. The fraction of atoms lying on the surface increases with decreasing particle size and enhances the chemical reactivity. Therefore, nanoparticles are also used as more effective catalysts in chemical reactions [21]. Also, the ability to transfer charge increases in small particles and make them useful in various electrochemical applications [22].

1.3.4 Electronic properties

The conductivity of materials is affected by several factors such as temperature and particle size. In solids, the electrical conductivity is defined by band structure. The separation between valence and conduction bands is called the energy band gap. Due to a size reduction, the quantum size effects change the band gap. It leads to an increase in band gap of metals and semiconductors that decreases the conductivity of nanoparticles. The density of states in these bands is reduced and replaced by quantized levels [23]. The quantization of levels is size-dependent and affects the electrical behaviour of nanoparticles. Quantum dots show an effect called the Coulomb blockade. In this, the current flow is not observed till the applied voltage reaches $\frac{e}{2C}$, where C is the capacitance. The current flow increases in steps of $n\frac{e}{2C}$, where $n = 1, 2, 3, ...$ [24].

1.3.5 Mechanical properties

Mechanical properties, such as fracture toughness, fatigue resistance, scratch resistance, hardness, etc. are modified with decreasing particle size. Defects are more prominent in bulk materials than smaller particles. Therefore, nanoparticles have lesser defects and so high mechanical strength. The yield strength of materials is described by the Hall Petch equation

$$\sigma_y = \sigma_o + \frac{k}{\sqrt{D}}, \tag{1.7}$$

where σ_y is yield strength, σ_o and k are material constants defining resistance towards dislocations and strength, respectively, D is the diameter of particles or grains. Ceramics are generally hard and brittle but with the reduction in grain size they can easily be pressed and sintered. The hardness of Cu/Nb nanocomposite becomes four times greater than their bulk form [10, 20].

1.3.6 Magnetic properties

The occurrence of different magnetic behaviour as the particle goes from multi-magnetic-domain to single-magnetic-domain is an intrinsic property. The magnetic characteristics exhibited by single-magnetic-domain are different from their micro or bulk counterparts. Decreasing size causes different surface and volume energy compared to macro materials. At the nanoscale, the boundary conditions of the system change and no longer remain periodic. Superparamagnetism is one such interesting phenomenon observed in these systems [25]. This discovery has triggered research in the physics of magnetic nanoparticles. When thermal energy becomes larger than magnetocrystalline energy, the energy which is responsible for the alignment of spins in a particular direction, the magnetization vector is no longer fixed in a particular direction. The particle magnetic moment starts fluctuating randomly and the phenomenon is called superparamagnetism. In this state, the small particles collectively show large magnetic moment and display paramagnetic-like characteristics and are termed superparamagnetism. Magnetization of ferro or ferrimagnetic materials are observed to be decreased with decreasing size of the particles.

Small particles of magnetic materials have been extensively studied during the last few decades. Their studies have been amassed by their different properties and applications. Before understanding the magnetization in nanoparticles, we shall discuss crystal anisotropy.

1.4 Magnetocrystalline Anisotropy

The magnetization vector of particles remains fixed in a preferred direction called an easy axis. There is another direction along which it is most difficult to orient the magnetization vector. It is called the hard axis. The energy associated with the orientation of the magnetization vector with respect to the easy axis is called magnetocrystalline

anisotropy energy. This energy has the lowest value if the magnetization vector remains along the easy axis. The magnetization vector can be rotated in a controlled manner by the application of an external magnetic field. The thermal energy causes the magnetization vector to flip in an uncontrolled manner. Magnetic anisotropy in crystals is determined by the spin-orbit coupling of electrons. This is one of the main factors that affect the shape of magnetization curves. It simply means that there is a direct strong dependence of magnetization along some preferred direction. It is important to consider anisotropy in magnetization studies because most commercially designed materials make use of it. That is why thorough information about magnetic anisotropy is important for understanding its practical uses. There are many forms of crystal or magnetic anisotropy. The magnetocrystalline anisotropy energy per unit volume for a cubic system in a crystal is given by [1]

$$E_{cubic} = K_0 + K_1(\alpha_1^2\alpha_2^2 + \alpha_2^2\alpha_3^2 + \alpha_3^2\alpha_1^2) + K_2(\alpha_1^2\alpha_2^2\alpha_3^2) + ----, \tag{1.8}$$

where K_0, K_1, K_2, ... are anisotropy constants and α_1, α_2, α_3 are the directions consines which saturation magnetization makes with cubic directions. The simplest form of crystal anisotropy is uniaxial anisotropy. In this case, the system has only one preferred direction. Hexagonal cobalt is one such system. Here, the c axis is the easy axis and any axis that lies within the plane perpendicular to it is a hard axis as shown in Fig. 1.1.

The magnetocrystalline anisotropy energy for an uniaxial system in a crystal is given by [5]

$$E_{an} = -(K_2V\cos^2\beta + K_4V\cos^4\beta + K_6V\cos^6\beta + ----), \tag{1.9}$$

where K_2, K_4, K_6, ... are anisotropy constants, β is the angle between $\vec{\mu}$ and the

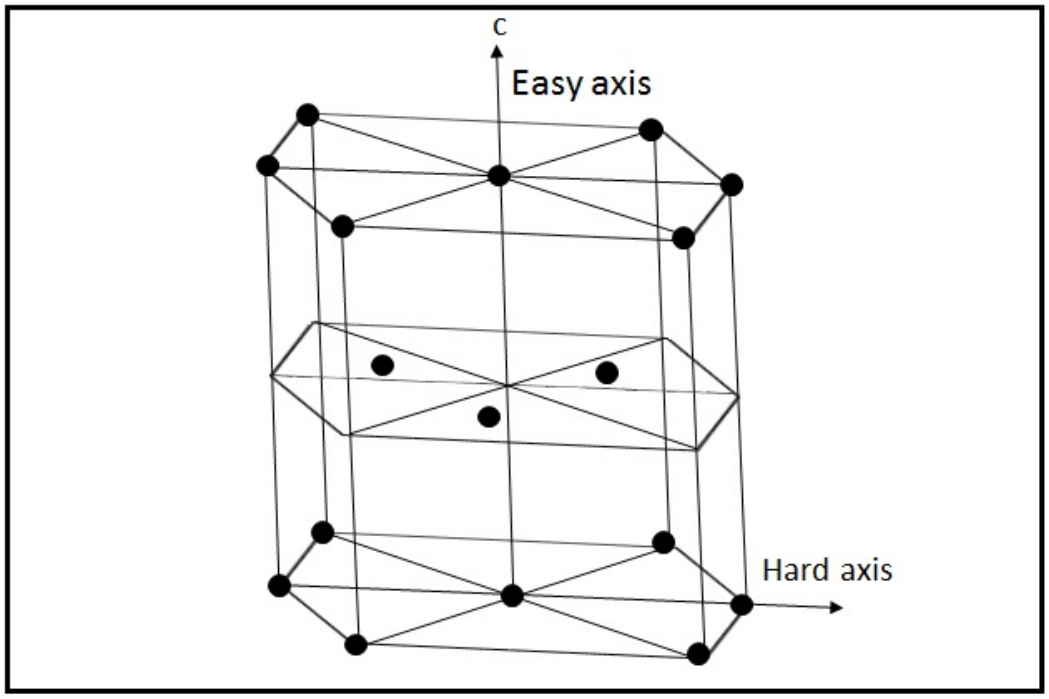

Fig. 1.1: Easy axis of a hexagonal unit cell.

easy axis unit vector $\vec{e}$ and V is the volume of the particles. Usually, the first term of anisotropy energy is most significant. Putting $K_2 = K$, the expression for magnetocrystalline anisotropy energy in an uniaxial system takes form

$$E_{an} = -KV \cos^2 \beta. \tag{1.10}$$

This expression clearly shows that anisotropy energy is dependent on the volume of the particle. Figure 1.2 shows variation of anisotropy energy E_{an} as a function of angle β, the angle between the magnetization vector and the c axis. As the magnetization vector rotates away from the easy axis, the anisotropy energy increases with increasing β. The anisotropy energy takes its maximum value for $\beta = 90^o$ and then starts decreasing for any further increase in β. It then takes its original minimum value for $\beta = 180^o$. From Fig. 1.2, it is clear that the height of the energy barrier between two minimum energies is KV. This energy barrier can be overcome by the application of

magnetic field and temperature.

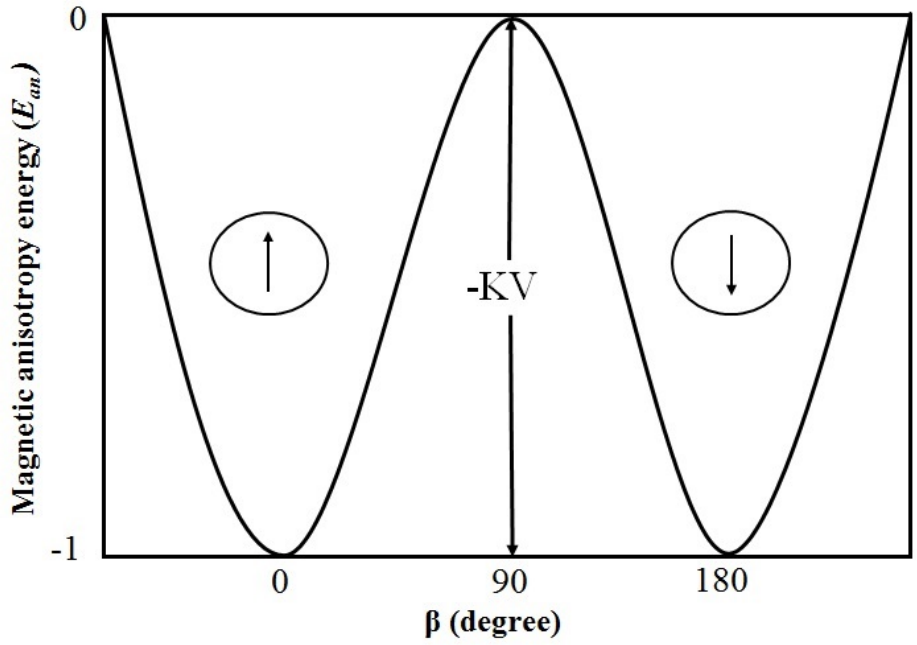

Fig. 1.2: Magnetocrystalline anisotropy energy E_{an} as a function of angle β for an uniaxial system.

There are many methods for determining the magnetic anisotropy constant i.e. torsion pendulum, torque curves, magnetization curves, and magnetic resonance [1].

1.5 Superparamagnetism

The unique and interesting observations exhibited by small magnetic particles make them the subject of intensive research [16, 26]. These particles have owned an important place in the field of science and technology with emerging applications in magnetic storage media, biomedicines, electronic devices, etc. [10, 11, 13]. According to Néel and Brown, an ensemble of nanoparticles with weak or negligible interactions shows superparamagnetic behaviour [27, 28]. The magnetization process in ferro or ferrimagnetic materials is well studied in the superparamagnetic region. Bulk forms of these materials show hysteresis loops in magnetization M as a function of the applied magnetic field

B curve below the Curie temperature T_c. These materials consist of magnetic domains which are separated by domain walls. These domain walls arise because the materials tend to have minimum possible energy. Therefore, these systems have multi-domains, each has spins aligned in a particular direction. Due to it, their magnetization is accompanied by rotation of domain walls and they show hysteresis on the application of the magnetic field. These materials have large magnetization. With the reduction in particle size, the saturation magnetization of these systems decreases because of disordered atoms on the surface [29]. Within nanometre range, below a certain size, no domain walls are formed and the particle magnetic moment participates in rotation. At high temperature, the orientation of the particle moments is not stable and fluctuates quickly in random directions. Thus, these materials no longer retain the hysteresis curve and their remanence is zero. This displays the superparamagnetic character. It was assumed earlier that only small particles of ferro and ferrimagnetic materials show superparamagnetism [25]. But later on, nanoparticles of antiferromagnetic materials were also found to show this similar characteristic. Bulk antiferromagnetic materials possess zero net magnetic moment. But for small particles, the disordered moments on the surface of atoms contribute to magnetization whereas the core does not have any contribution. Therefore, in antiferromagnetic particles, the magnetization decreases with increasing particle size [30]. The origin of magnetic moment in antiferromagnetic materials is explained by two sublattices model.

The bulk crystals of antiferromagnetic materials consist of two sublattices [2]. In one dimension system, each sublattice has a parallel alignment of magnetic moments but both the sublattices have magnetic moments arranged in opposite directions. Due to these equal and opposite magnetic moments, the net magnetization is zero in the absence of a magnetic field and at temperature $T = 0\ K$. However, this is not always the case as the number of opposite magnetic moments needs not to be exactly equal and the material possess a net magnetic moment. In two dimensional system, a missing

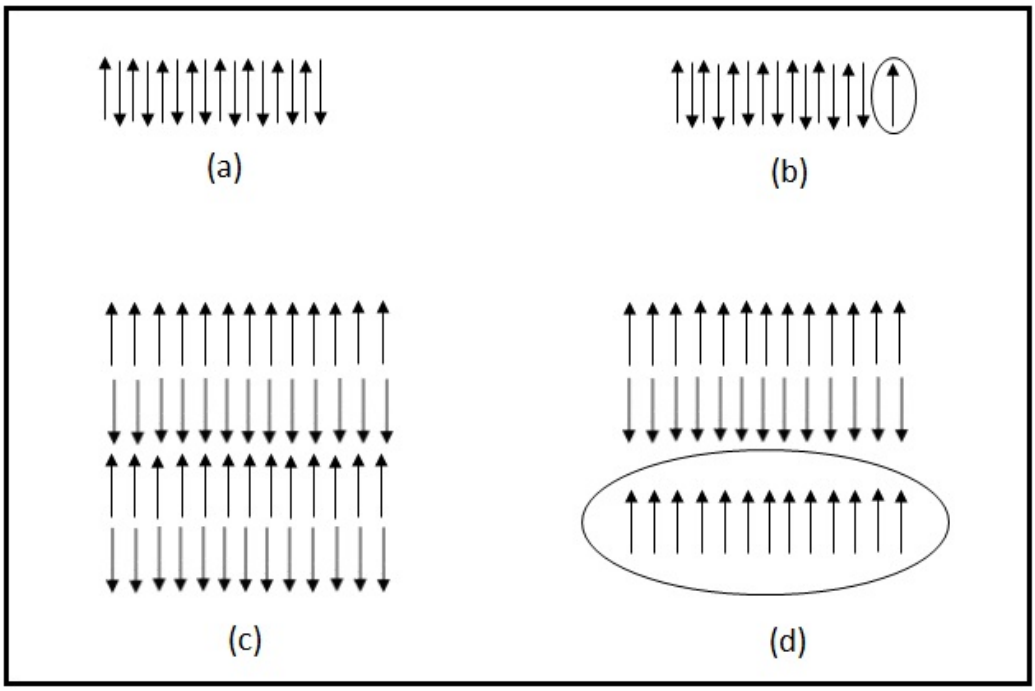

Fig. 1.3: Antiferromagnetic ordering of magnetic moments (a) in one-dimensonal system with zero net magnetic moment, (b) system shows magnetic moment due to incomplete cancellation of spins, (c) in two dimensional sytem with zero net magnetic moment, and (d) one layer of spins is missing showing net magnetic moment.

layer of spin contributes to some magnetic moment in antiferromagnetic materials. The explanation for it is shown in Fig. 1.3. Similar is the case for a three-dimensional system.

The magnetization process inside material is well explained by its temperature, applied magnetic field, and time dependence. We shall now concise our discussion to analyse how the relaxation mechanism and spin orientation contribute to magnetization behaviour under the effect of these factors in the superparamagnetic region.

1.5.1 Behaviour of superparamagnetic particles

In superparamagnetic particles, the magnetization vector flips randomly between energy minima when thermal energy becomes larger than the anisotropy energy. The

probability with which magnetization vector changes its orientation by crossing energy barrier KV is $\exp(-\frac{KV}{k_BT})$. This probability is directly proportional to the frequency with which the magnetization vector fluctuates. Thus, the magnetization dynamics of superparamagnetic systems are described by Eq. (1.11). Here, ν is the frequency with which the magnetization vector fluctuates between energy minima. This is known as Néel-Arrhenius law.

$$\nu = \nu_0 \exp(-\frac{KV}{k_BT}), \tag{1.11}$$

where ν_0 lies in between 10^8 to 10^{12} Hz [31]. The relaxation time of these random fluctuations is described by

$$\tau = \tau_0 \exp(\frac{KV}{k_BT}). \tag{1.12}$$

Clearly, the relaxation time depends on the volume V of the magnetic nanoparticles. The presence of volume defines a particular size of the particle for the superparamagnetic transition to occur at a threshold temperature. There is always a narrow or broad distribution in particle size in a sample of nanoparticles. Particles with relaxation time order of experimental observation time contribute to the magnetization process. The relaxation time has a great impact on magnetic behaviour. If the relaxation time of particles is greater than the experimental measurement time (τ_m) i.e. $\tau \gg \tau_m$, then the particle magnetic moment appears to be blocked along with its preferred orientation. This state is called a blocked state. But, when the relaxation time is less than the experimental measurement time then the magnetization vector of the particle observe to be fluctuating randomly and the average orientation of the magnetic moment appears to be zero in the given experimental time window. The particle in this state behaves like paramagnetic with giant susceptibility and is called superparamagnetic. These magnetization measurements can be done by fixing and varying experimental observation time. During dc magnetization measurements, the frequency of the signal is not varied and has a fixed value of experimental observation time of 100 s. It occurs

for $\tau_0 = 10^{-11}$ s. In ac magnetization measurement, the experimental observation time can be varied by changing the frequency of the applied magnetic field.

The relaxation process of spins in magnetic systems is greatly affected by applying external perturbations. Information about the response to the external perturbations gives a clearer picture of the magnetization in materials. Magnetization as a function of temperature and applied magnetic field data are used to study the magnetic behaviour of magnetic particles. Figure 1.4 represents the measurement of susceptibility χ as a function of temperature T by cooling sample in the presence and absence of applied magnetic field for superparamagnetic particles. These curves are quite informative. In zero field cooled susceptibility measurement, firstly, the sample is cooled to low temperature in absence of an external magnetic field while in field cooled measurement the temperature of the sample lowers in the presence of an external magnetic field. After this, a small magnetic field is applied and data is collected with increasing temperature. During ZFC susceptibility measurements, at low temperature and zero applied magnetic field, the magnetic moments are aligned randomly along their easy axis. When a low magnetic field is applied the moments slowly try to rotate along the magnetic field and result in small magnetization in the sample. As the temperature rises, the magnetic moments start relaxing along the magnetic field, and magnetization increases with increasing temperature. The increase in temperature causes a decrease in the relaxation time of flip. After the further increase in temperature, the magnetization reaches a peak point and saturates. At this point, the relaxation time of particles becomes equal to the measurement time scale of the experiment i.e. $\tau = \tau_m$. The temperature at which the peak point occurs in the ZFC curve is called blocking temperature T_B. In the vicinity of blocking temperature, the thermal energy becomes almost equal to anisotropy energy and blocking temperature is given as $T_B = \frac{KV}{25k_B}$. The blocking temperature T_B is the same for the individual particle in a system of non-interacting particles of uniform size. If the system is polydispersed, then there

is always a distribution of blocking temperature that arises due to the distribution in particle size. Above blocking temperature, the particle magnetic moment relaxes fast and thermal energy overcomes the energy barrier. The orientation of particle magnetic moments fluctuate randomly between two energy minima and magnetization of the system starts decreasing. In this region, the coercivity of the system and the area under the M-B loop becomes zero because of the fast relaxation of the particle. These are the characteristics of a superparamagnetic system. During the FC susceptibility

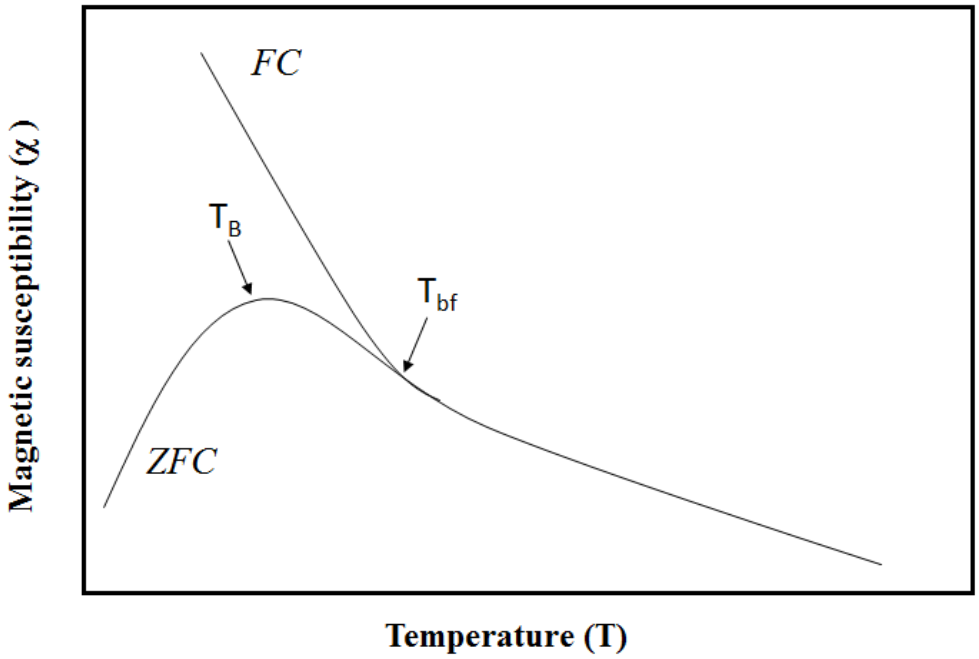

Fig. 1.4: Zero field cooled (ZFC) and field cooled (FC) susceptibility curves for superparamagnetic system.

measurements, an applied field is present while cooling the sample to low temperature. There are two types of FC curve measurements (a) field cooled cooling (FCC) (b) field cooled warming (FCW). During FCC, the measurements are done during cooling and in FCW mode, the sample is cooled in the presence of some magnetic field and the measurements are taken with increasing temperature. At low temperatures, the magnetic moments aligned more towards the magnetic field direction and shows

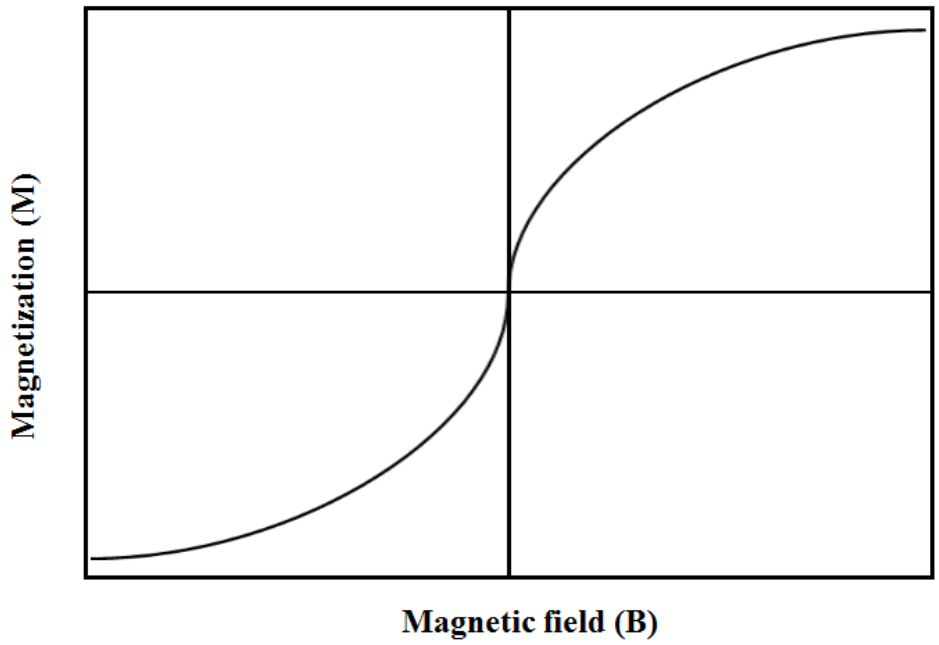

Fig. 1.5: Magnetization M as a function of applied magnetic field B for superparamagnetic system.

large susceptibility. Briefly, ZFC and FC curves display some features (a) both curves merge at high temperature and shows a paramagnetic like character (b) when lowering temperature susceptibility increases until a point reached where these curves diverge due to the magnetic anisotropy and the temperature at this point is called bifurcation temperature T_{bf}. After that, susceptibility in the FC curve still rises gradually but the ZFC curve exhibits a peak called blocking temperature, and susceptibility decreases with further lowering the temperature.

An external applied magnetic field also affects the relaxation process and the overall behaviour of magnetic materials changes because the magnetic moments try to align along the field direction. M-B loop also depicts the characteristics of the superparamagnetic system. The magnetization M versus applied magnetic field B loop for superparamagnetic particles is shown in Fig. 1.5. The shape of this loop depends upon the region of temperature measurement. If the measurements are done below

the blocking temperature T_B, the magnetic moments relax slowly and display an area under the M-B curve. Above blocking temperature, the relaxation time decreases and the area under the M-B curve shrinks to zero. The magnetization of magnetic nanoparticles increases with an increase in the magnetic field.

In 1961, Néel reported that antiferromagnetic materials also show superparamagnetism as their particle size reduces to nanometer range [27]. In superparamagnetic region, the magnetic behaviour of ferro or ferrimagnetic particles is different from antiferromagnetic systems. Magnetization as a function of applied magnetic field of these systems in superparamagnetic region is described by Langevin equation given as

$$M(B,T) = M_0 L(x), \tag{1.13}$$

where M_0 is saturation magnetization, $L(x) = [\coth(x) - (\frac{1}{x})]$ is the Langevin function, $x = \frac{\mu B}{k_B T}$, μ is particle magnetic moment and k_B is the Boltzmann constant. The magnetization of ferro or ferrimagnetic nanoparticles saturates at higher fields. But in antiferromagnetic systems, the magnetization does not saturate at higher fields, but increases linearly. The slope of curve in linear region gives antiferromagnetic susceptibility of particle cores. Therefore, this equation is different for antiferromagnetic system and the magnetization process in antiferromagnetic particles in superparamagnetic region is described by adding an extra linear term in B in Eq. (1.13) as

$$M(B,T) = M_0 L(x) + \chi B. \tag{1.14}$$

Here χ is the antiferromagnetic susceptibility of particle core. This equation is called as modified Langevin equation.

1.5.2 Applications of magnetic nanoparticles

The magnetic behaviour of nanoparticles is an area of wide interest because of their enormous applications. Their remarkable features are the reason for their beneficial applications as follows:

- Drug delivery using magnetic nanoparticles has an advantage over most chemotherapies. Magnetic nanoparticles directly release drugs inside the body to tumor cells [17]. The magnetic forces are capable of administering the drug to a specific area without any side effects. For this purpose, biocompatible magnetic nanoparticles are attached to the drug and a magnetic field gradient is applied. With the help of magnetic force, the nanoparticles act as vehicles to direct the transfer of the drug to the targeted area. Biocompatible materials like iron oxide nanoparticles are commonly used for drug delivery.

- Nanoparticles of magnetic materials are used for bioseparation of molecules, cells, proteins, DNA due to their extremely small size compared to the size of biological entities [32, 33]. The biological entity which is to be separated is tagged with magnetic nanoparticles and separated on the application of magnetic force [17].

- One of the remarkable use of magnetic nanoparticles in biomedicines is hyperthermia, which is proved to be a boon in the medical field. These particles are used in the treatment of invasive tissues. Cancer cells and tumors are sensitive to high temperatures. Magnetic nanoparticles activate in the presence of a magnetic field and heated at desired temperature using the alternating external magnetic field [17, 34]. These are assumed to be good candidates for treating cancerous tumors as they can be magnetically guided to the affected area without damaging the healthy cells.

- Magnetic nanoparticles are also found to be promising candidates for clinical di-

agnosis. Magnetic resonance imaging (MRI) is a widely used diagnostic technique for detecting the structure and function of tissues [35]. In this technique, magnetic nanoparticles are used to make contrast and widen the diagnosis of specific tissues.

- Magnetic nanoparticles are also used for magnetic recording and information storage [7]. The stability of magnetic data storage depends upon the magnetic anisotropy energy. Large magnetic anisotropy is required for the storage medium to withstand thermal fluctuations, otherwise, it will lead to loss of information.

- Due to small size, the increased surface area of magnetic nanoparticles enhances their catalytic activity [21]. Therefore, these particles are used for increasing the reaction rate.

- Nanoparticles of magnetic materials are also used as biosensors. Bioanalysis of cells, proteins, or biomolecules with good sensitivity can be done using magnetic nanoparticles [36].

1.6 Literature Review and Motivation

Many works have been carried out to understand the magnetic behaviour of small particles for the past few years. The rotation of magnetic moment plays a crucial role in the magnetization of nanoparticles. Two mechanisms are known as Néel and Brownian relaxations explain magnetic rotations in these systems [28, 37]. According to Néel model, the magnetization vector of particle aligned in a specific direction and fluctuate in up and down state under the influence of external energies. But, in Brownian relaxation theory, external energies rotate the whole particle [38]. These rotations are affected by external parameters temperature and magnetic field which are responsible for providing thermal energy and Zeeman energy, respectively. Earlier,

we have discussed, the dependence of relaxation time on these energies. Particle magnetic moment relaxes slowly in low-temperature region [25,39]. At higher temperature, the relaxation of particle magnetic moments appear faster and the magnetization of the system reaches equilibrium. This region represents the superparamagnetic state of nanoparticles. Nanoparticles of ferro and ferrimagnetic materials were extensively studied in this region during the last few decades [25]. The unique behaviour exhibited by these particles was the reason for their popularity among researchers. These small particles are used in various technological applications [17, 40]. The magnetization of these systems was well described by several authors by Eq. (1.13) [16].

Later on, it was discovered that antiferromagnetic nanoparticles exhibit different behaviour compared to ferro or ferrimagnetic systems. Researchers found that magnetization in antiferromagnetic particles did not follow Eq. (1.13) in superparamagnetic region. In 1995, Kilcoyne studied the magnetization of antiferromagnetic ferritin nanoparticles and found that the magnetization of ferritin is described by the Langevin equation after adding an extra linear term in B [41]. After adding this term, the equation is called modified Langevin equation i.e. Eq. (1.14). In 1997, it was reported that magnetization vs applied magnetic field data of antiferromagnetic systems ferritin and NiO in the superparamagnetic region was well-fitted with modified Langevin equation [42,43]. Later on, groups of researchers investigated the magnetization of antiferromagnetic nanoparticles system using this equation [44–48]. The anomalies were always found using the modified Langevin equation alone, due to the non-consideration of several factors. Because this equation is based on assumptions that all particles have the same size and magnetic anisotropy energy is zero. Researchers suggested including a log-normal distribution in particle magnetic moment in the modified Langevin equation. In 2005, Silva et al. fitted the magnetization curves of ferritin samples using modified Langevin equation and found inappropriate values of fit parameters [48]. Also, scaling-law is used to study the temperature dependence of magnetic parameters such

as magnetic susceptibility and mean uncompensated moment. Then, they analysed magnetization data considering a log-normal distribution in the magnetic moment and found physically meaningful fit parameters. The decrease in particle size leads to surface disorders, magnetic frustrations, and spin canting which result in uncompensated magnetic moment. The contribution of the thermo-induced magnetic moment was also assumed to be responsible for the observed increased magnetic moment with temperature in the studies [49]. Several other authors also concluded that the consideration of particle magnetic moment distribution is important while analysing the magnetization data of any nanoparticle system [48, 50–57]. Magnetic anisotropy is another important factor that affects the magnetization in nanoparticles [5, 58–60]. Madsen et al. studied the effect of magnetic anisotropy on the magnetization of antiferromagnetic nanoparticles and concluded it as a necessary parameter for analysing magnetization data of nanoparticles. But, the simultaneous effect of magnetic anisotropy and particle size distribution has not been studied. This motivated me to work on this issue. This thesis presents detail magnetic investigations on naturally occurring antiferromagnetic ferritin and laboratory synthesized NiO nanoparticles. The objectives of this thesis are

- Structural and morphological characterization of iron storage protein ferritin and NiO.
- Thermal characterization by TGA.
- Measurements of magnetization M as function of temperature T and applied magnetic field B.
- Analysis of magnetization data.

Ferritin is an iron storage protein found in the blood of mammals [61]. The 7-8 nm core of this molecule is shielded by a 2-3 nm thick protein shell [62]. This shielding is the reason for the reduction in strength of dipolar interactions among particles and

makes this system a model superparamagnetic [41]. The ferritin core consists of ferric-oxyhydroxide-phosphate complex having molecular formula $(FeOOH)_8[FeOOPO_3H_2]$ [63]. Many studies were attempted to find the crystal structure of ferritin but to date, it is not understood clearly [61,63–65]. But, the major phase of its core is reported similar to mineral ferrihydrite ($FeOOH{\cdot}nH_2O$) [66]. Ferrihydrite is one of the main ore of the iron oxide family [67]. Magnetization studies and thermal behaviour of ferrihydrite are well-reported [44–46, 54, 68–73]. But still, its disputed crystal structure is a subject of concern [74]. Some other studies claimed the presence of other phases along with ferrihydrite which is still an ambiguity [62,65,75,76]. Some authors reported the study of iron oxide particles synthesized from ferritin core by heating it at arbitrarily different temperatures [77, 78]. Ferritin cores have almost uniform size and narrow particle size distribution. On the other side, NiO is also an antiferromagnetic system, and its magnetic behaviour was extensively studied by different authors [30,43,51,79–84]. The synthesized NiO samples have wide particle size distribution. In this way, we are motivated to analyse the magnetization data of these two systems by considering the presence and absence of magnetic anisotropy. Also, the effect of narrow and wide particle size distribution in the magnetization process has been established.

Chapter 2

EXPERIMENTAL DETAILS

In this chapter, processing of ferritin sample, synthesis of nickel oxide nanoparticles and working principle of used characterization techniques are discussed.

2.1 Sample Preparation

Nanoparticles of different materials are usually prepared by suitable physical and chemical methods [10]. Popular physical methods are inert gas condensation, laser pyrolysis, flame spray pyrolysis, physical vapour deposition etc. whereas popular chemical methods are sol-gel synthesis, hydrothermal method, co-precipitation, polyol synthesis etc. One can control shape, size and distribution by regulating few parameters during the process. Chemical reactions take place at the atomic or molecular level. Due to this, it is easy and convenient to control particle morphology following chemical routes for the synthesis of nanoparticles. These methods also have added advantage of being cheap in comparison to physical methods. There are also few nanoparticles systems found in nature. Ferritin is one such example. It is found in the blood of living organisms [61]. This thesis is based on the structural, thermal, and magnetic characterization of ferritin and NiO nanoparticles.

Ferritin: A 100 ml sample of ferritin from the equine spleen is purchased from Sigma Aldrich Corporation, USA in form of a 0.15 M saline suspension. The salinity controls the osmosis pressure and protects the blood cells from being damaged. A

diluted form of this suspension is used for transmission electron microscopy. The original suspension is dried under vacuum (5×10^{-4} torr) at room temperature. The dried brown coloured flakes are ground to get fine powder of ferritin. This powder sample of ferritin is used for further characterization.

Nickel Oxide Nanoparticles: Nickel hydroxide powder is synthesised by a chemical method [30, 82, 85]. For this, a 4 M aqueous solution of sodium hydroxide is added dropwise to a 0.5 M aqueous solution of nickel nitrate hexahydrate, while continuously stirring, till the pH of the solution reaches 12. The used chemicals are purchased from Sigma Aldrich Corporation, USA. The resulting green precipitate is washed several times with distilled water. It is dried at 100 ^{o}C. The dried flakes are ground to get a fine powder of nickel hydroxide. This powder is heated at 250 and 300 ^{o}C for three hours in an inert atmosphere to get NiO particles.

2.2 Experimental Techniques

In the present work, the samples are characterized by an x-ray diffractometer, transmission electron microscope, thermogravimetric analyzer and vibrating sample magnetometer. Working principles of these techniques are described below.

2.2.1 X-ray diffractometer

X-ray diffractometer is used for the determination of the crystal structure of materials. Crystalline solids consist of sets of parallel atomic planes. These planes are at a separation of few angstroms. So, the radiation used for diffraction must have a wavelength of few angstroms. Due to this, x-rays are used for this purpose. These radiations can also penetrate deep inside the crystal.

If a monochromatic parallel beam of x-rays of wavelength λ is incident on a set of parallel atomic planes then the reflected rays undergo constructive interference if $2d \sin\theta = n\lambda$, where d is interplanar distance, θ is the Bragg angle and $n = 1, 2, ...$

It is known as Bragg's law [2]. The value of n indicates the order of diffraction. The intensity of the diffracted beam decreases with an increase in order. Because of this reason, we usually observe only first-order diffraction pattern in a conventional x-ray diffractometer.

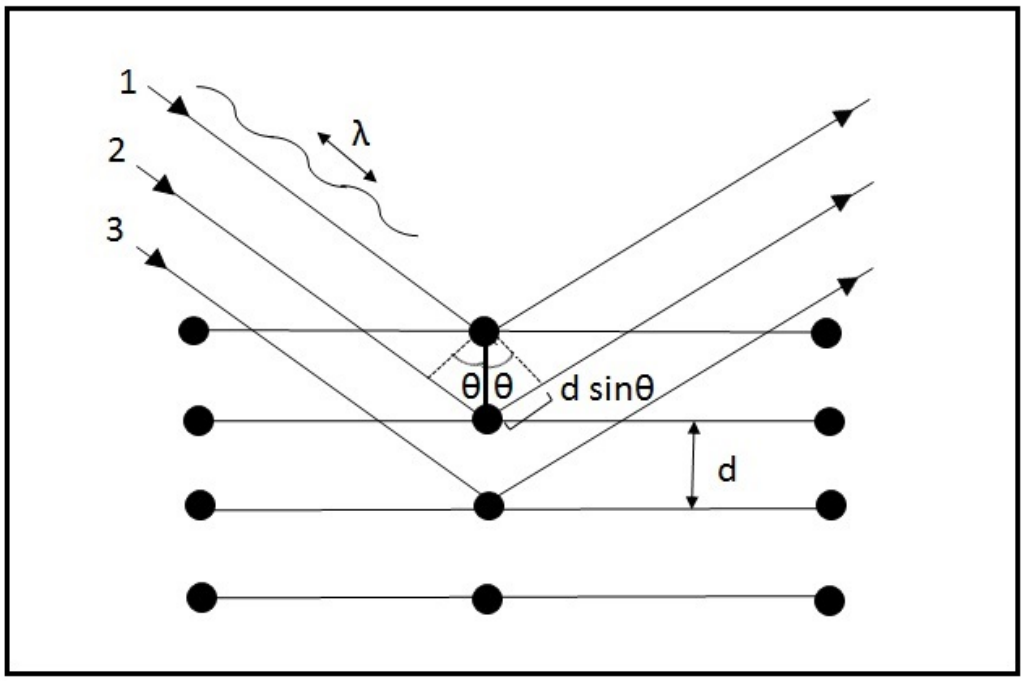

Fig. 2.1: X-ray diffraction from parallel atomic planes.

A powder x-ray diffraction pattern consists of several peaks. Each peak corresponds to a Bragg reflection from a particular set of the parallel atomic plane. The diffraction peaks have finite broadening. Instrument, non-uniform lattice strain and crystallite size are responsible for this. The lattice strain can be avoided by controlling suitable parameters during sample preparation. The crystallite size t and line broadening B_M are related by Scherrer formula as [86]

$$t = \frac{0.9\lambda}{B_M \cos\theta}. \tag{2.1}$$

Here B_M is the width where intensity is half of its peak value. It is called full width

at half maximum. This equation shows that the crystallite size is inversely proportional to the line broadening. But, this equation does not consider the role of instrumental broadening. However, if we subtract full width at half maximum B_S of the same peak in the x-ray diffraction pattern of a standard bulk sample then the effect of instrumental broadening can be avoided [86]. So, a modified form of the Scherrer formula which takes care of the instrumental broadening is

$$t = \frac{0.9\lambda}{\cos\theta(B_M - B_S)}. \tag{2.2}$$

This form of the Scherrer formula assumes that the diffraction peaks have Lorentzian nature. If the diffraction peaks have Gaussian nature then the term $(B_M - B_S)$ is replaced by $\sqrt{B_M^2 - B_S^2}$.

A PANalytical X'Pert Pro x-ray diffractometer has been used to characterize powdered samples in the present work.

2.2.2 Thermogravimetric analyzer

Sometimes materials are susceptible to heat and change their phase on heating. During this process, the materials may undergo physical and chemical changes. In this instrument, the material is heated at a constant heating rate in the air or any other specific environment [87]. The change in mass of the sample is recorded as a function of temperature and time. The results of the analysis give information about loss of water and solvent, vaporisation, sublimation, decarboxylation, oxidative stability, decomposition, pyrolysis. Also, the mass changes that occur during heating are used to calculate the weight fractions of components of the sample. Several instrumental and sample related factors may affect the results of the analysis. For example, heating rate, the mass of the sample, particle size, thermal conductivity, the geometry of pan, furnace atmosphere and gas flow rate etc. One can easily optimize these factors for

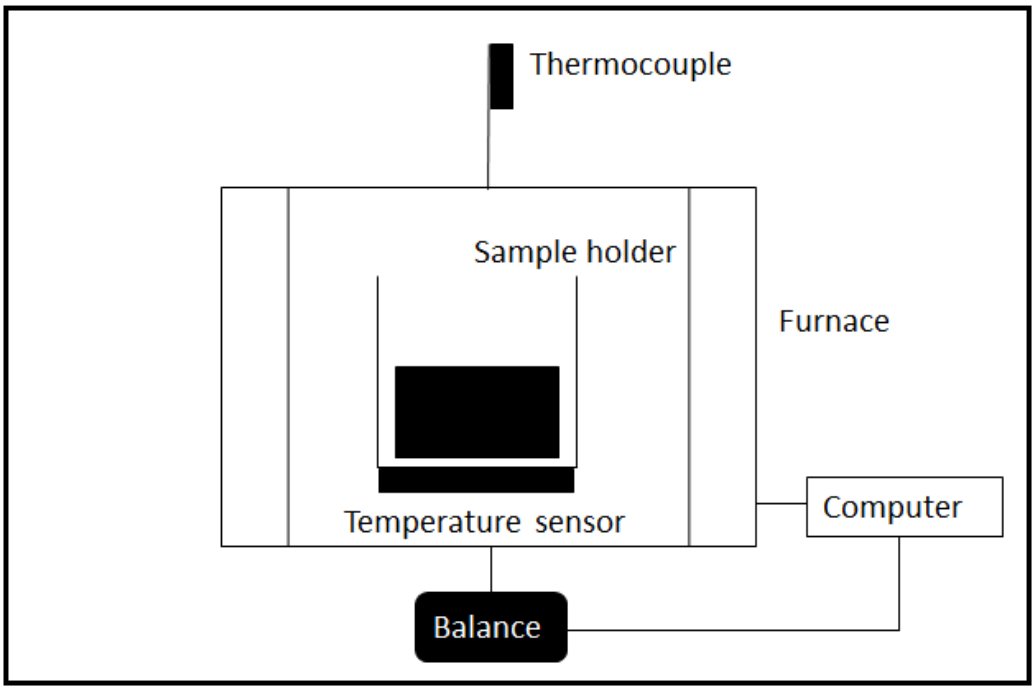

Fig. 2.2: Schematic representation of thermogravimetric analyzer.

highly reproducible results.

In present work, NETZSCH Jupiter thermogravimetric analyzer is used. Measurements are performed in air at a constant heating rate of 5 ^{o}C/minute.

2.2.3 Transmission electron microscope

Resolving power of any microscope is limited by phenomenon of diffraction. It dominates when separation between objects to be resolved becomes comparable to the wavelength of used radiation. Conventional optical microscopes use visible radiation and so these cannot resolve objects closer than 0.5 micron.

A transmission electron microscope uses a beam of energetic electrons [88]. Electrons can easily be accelerated by the application of a potential difference. The wavelength of associated de Broglie waves decreases with the increasing energy of electrons. Therefore, the resolving power of the transmission electron microscope increases with

increasing strength of applied potential difference for the acceleration of electrons. The wavelength λ of de Broglie waves and applied potential difference V are related as [86]

$$\lambda = \sqrt{\frac{150}{V}}. \tag{2.3}$$

If $V = 200$ kV then wavelength λ turns out to be 0.087 nm. It means one can resolve objects at a distance of 0.087 nm apart. Thus, the resolving power of a transmission electron microscope increases with an increasing potential difference.

This instrument operates in two modes. These are image mode and diffraction mode. Image mode gives information about the morphology of the particles and crystal planes. Diffraction mode works on Bragg's diffraction law. An electron diffraction pattern from many randomly oriented particles consists of concentric diffuse rings. Each ring corresponds to a particular set of parallel atomic planes and so a particular Bragg angle. One such pattern is shown in Fig. 2.3.

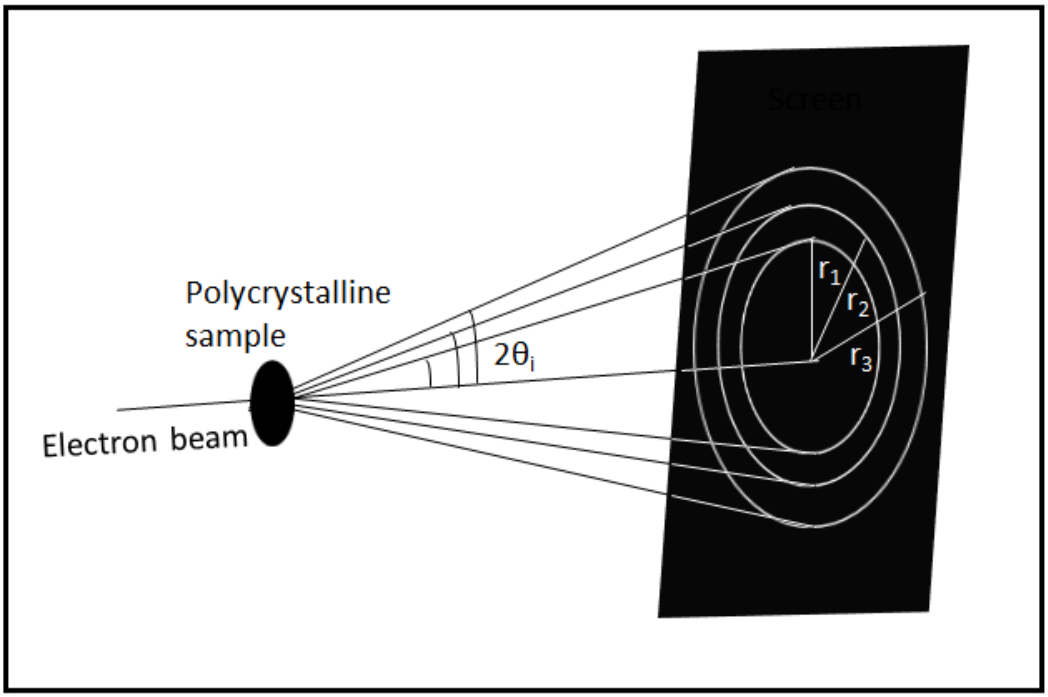

Fig. 2.3: Electron diffraction pattern from randomly oriented crystals.

In this work, JEOL JEM 2100Plus and FEI Tecnai transmission electron microscopes operating at a voltage of 210 kV have been used.

2.2.4 Atomic absorption spectrometer

It is an important technique to determine the concentration of an element in a given material. Commonly, the spectroscopy technique involves atomic emission or absorption which occurs due to the transition of valence electrons. In an electronic transition, under applied energies, an electron shifts from one energy level to another that involves the emission or absorption of radiations at particular frequency or wavelength, $\lambda = \frac{c}{\nu}$. For a specific electronic transition, the parameters ν and λ are unique. An element undergoes many electronic transitions and produces lines of spectra that identify the element. Atomic absorption spectroscopy involves the absorption of some optical radiation due to free atoms in a gaseous state. This technique follows Beer-Lambert law.

In this technique, when light falls on the gas phase of an element, the light of a particular wavelength at resonance is absorbed by its atoms. The output signal is directly proportional to analyte atoms [89]. As their number increases, the intensity of absorbed light also increases. In this way, the elemental composition of a given material can be determined. The sample under analysis is provided thermal energy to dissociate it into its chemical compound.

Before analysis, the sample preparation is necessarily done using digested methods. The digestion of the sample should be done with extreme care to obtain good results.

In this study, GBC Australia 932AA spectrometer has been used. The sample has been digested using nitric acid.

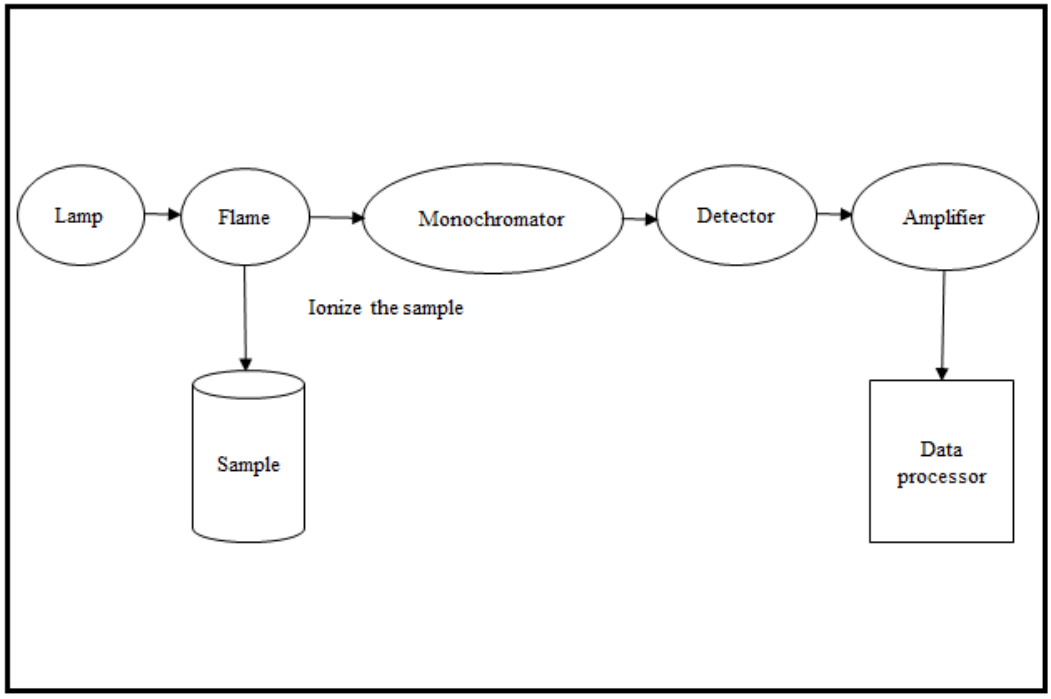

Fig. 2.4: Block diagram of atomic absorption spectrometer.

2.2.5 Vibrating sample magnetometer

To understand the magnetic behaviour of materials, one must know about their magnetic properties. Magnetic measurements are quite informative and can be measured by several methods [1]. A vibrating sample magnetometer (VSM) is an instrument used to determine the magnetic behaviour of materials. Magnetization measurements as a function of temperature and applied magnetic field are done using it. It works on the principle of Faraday's law of electromagnetic induction [90]. The VSM is a sensitive instrument and can be used to measure weak and strong magnetic moments. In VSM, the sample is placed between magnetic poles and a pickup coil in the sample holder. The sample holder is connected to a vibration exciter. This unit is responsible for the sinusoidal up and down motion of the sample at some frequency usually below 40 Hz. As the magnetized sample vibrates, an emf is induced in a near-by pickup coil. This emf is proportional to the magnetic moment of the sample. The pickup coil senses it

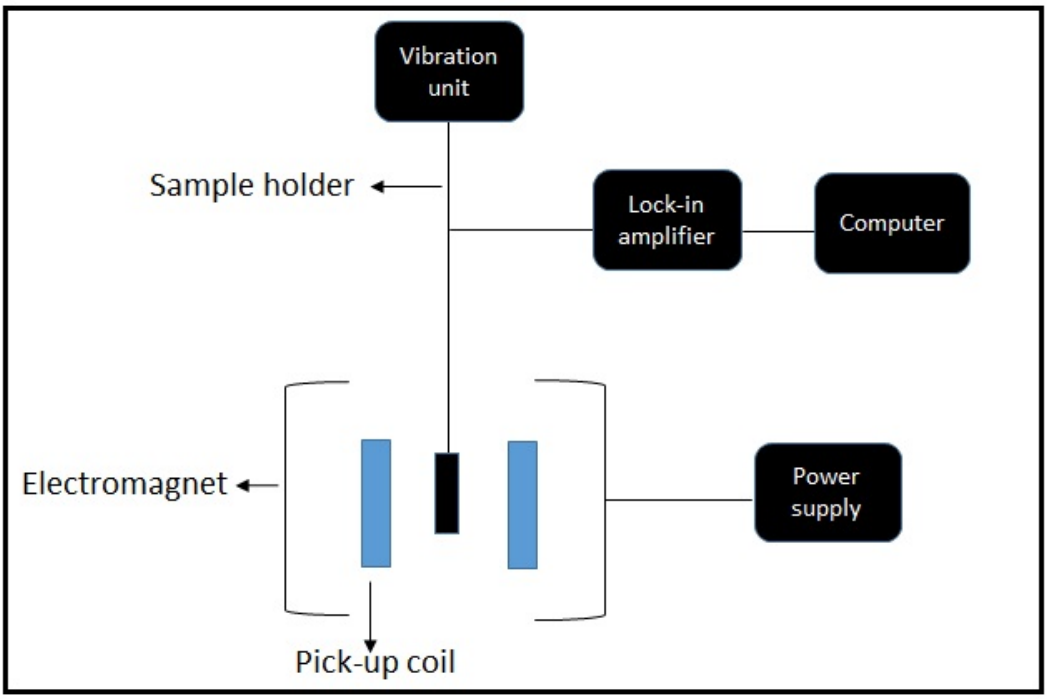

Fig. 2.5: Arrangement of electromagnets, pickup coils, vibration unit and output unit in vibrating sample magnetometer.

and the amplified electric signal is recorded using a lock-in amplifier.

In this work, a commercial vibrating sample magnetometer (Quantum Design, MPMS) has been used for magnetization measurement. The powder sample is tightly packed inside a non-magnetic capsule.

Chapter 3

FERRITIN NANOPARTICLES

In this chapter structural, thermal and magnetic characterization of ferritin nanoparticles are presented.

3.1 Structural Characterization

Figure 3.1 (a) shows x-ray diffraction pattern of ferritin at room temperature. Broadened diffraction peaks are due to poor crystallinity of the ferritin cores [63]. The ferritin cores also contain phosphate ions [66]. Ratio of iron and phosphate ions in ferritin core depends on its origin. The degree of crystallinity decreases with increasing concentration of phosphate ions in the system. The sharp peaks correspond to NaCl present in original suspension. The dried sample contains about 60 wt% NaCl. One drop of sufficiently diluted suspension is allowed to dry on a carbon coated copper grid for transmission electron microscopy. The obtained transmission electron micrograph of the sample is shown in Fig. 3.1 (b). Such micrographs show dense inorganic cores only [91]. Ferritin molecules are seen to be almost spherical in shape. The average core size is about 8 nm. Figure 3.1 (c) shows selected area electron diffraction pattern from ferritin particles. Two diffractions corresponding to two most intense peaks from

---

This chapter is based on following published works:

1. *Thermal decomposition of ferritin core*, Navneet Kaur and S. D. Tiwari, Applied Physics A: Materials Science & Processing **125**, 805 (2019).

2. *Role of Particle Size Distribution and Magnetic Anisotropy on Magnetization of Antiferromagnetic Nanoparticles*, Navneet Kaur and S. D. Tiwari, Journal of Physics and Chemistry of Solids **123**, 279 (2018).

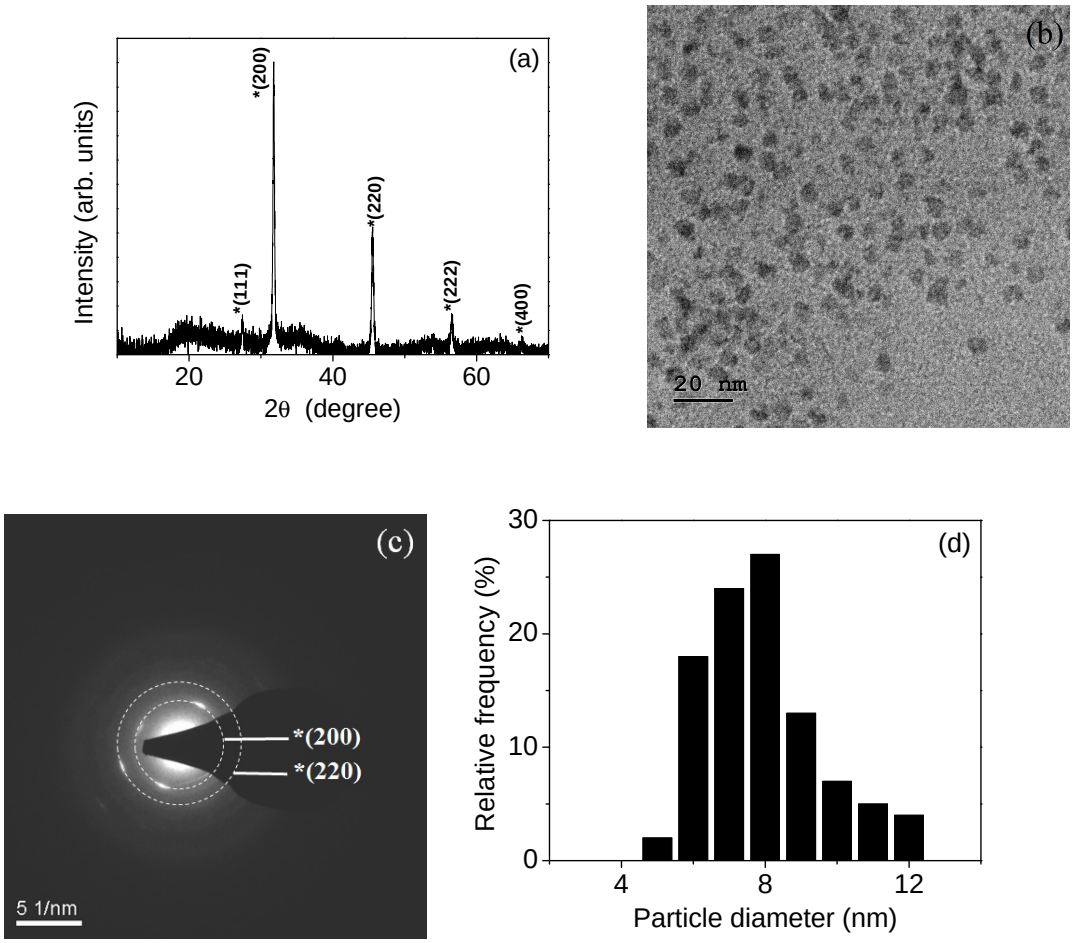

Fig. 3.1: (a) Room temperature x-ray diffraction pattern, (b) transmission electron micrograph, (c) selected area electron diffraction pattern and (d) a histogram of the distribution of particle size for ferritin. Bragg's reflections from ferritin are not detected. Dotted circles are visual guides. Indexed peaks and rings correspond to NaCl.

NaCl are clearly visible. Figure 3.1 (d) shows histogram for statistical distribution of particle diameter D. This distribution is based on size measurement of 100 particles. It peaks at 8 nm. The arithmetic mean of particle size is found to be 8.4 nm with a standard deviation of 1.6 nm. The sample is also characterized by atomic absorption spectrometer to determine concentration of iron. For this, the sample is digested in nitric acid. The iron concentration turns out to be 10 wt% in present ferritin sample.

Many compounds are not thermally stable and decompose to other compounds on

heating. Decomposition of ferritin is studied with thermogravimetric analyzer (TGA). For this, the sample is heated in air at constant heating rate of 5 ^{o}C per minute.

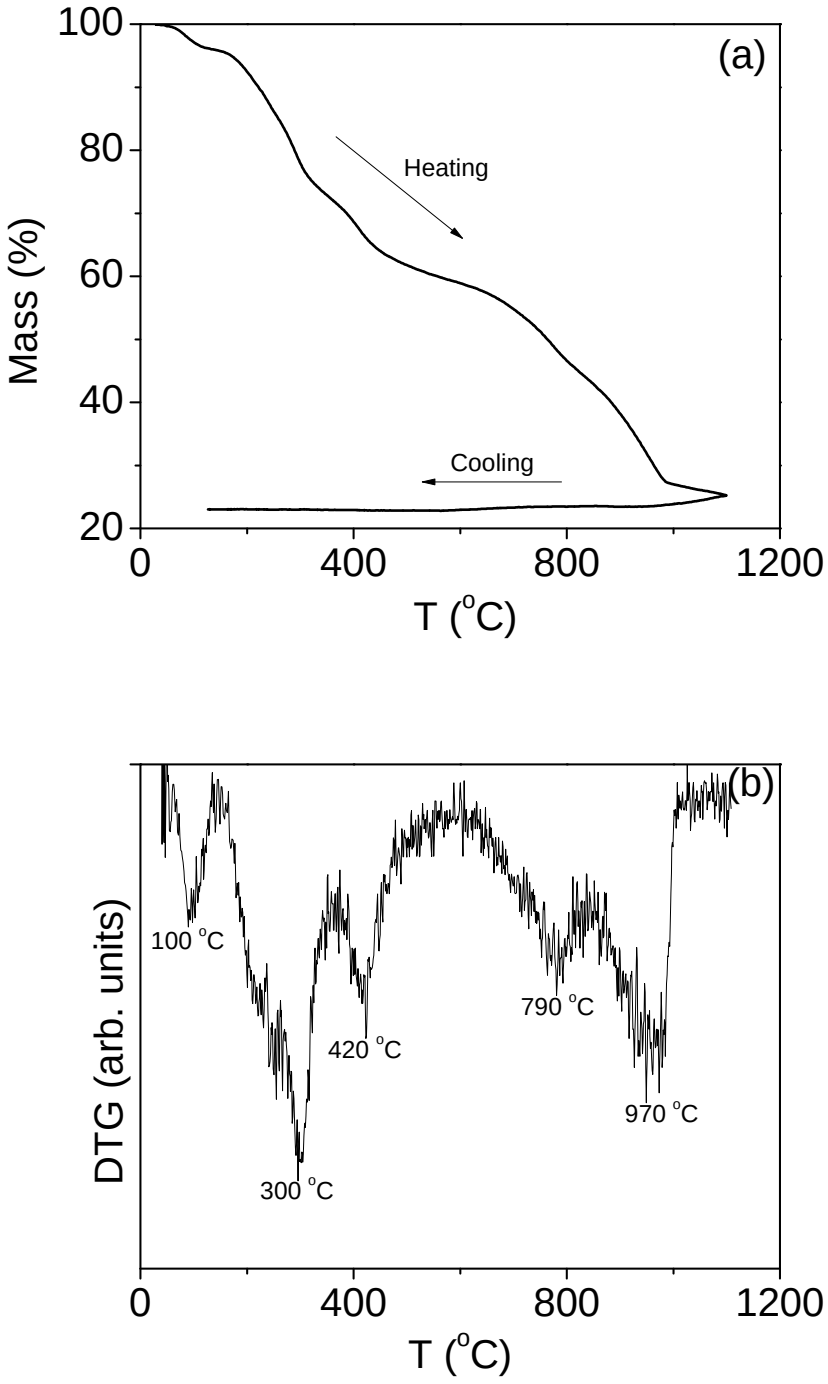

Fig. 3.2: (a) TGA and (b) DTG curves for ferritin.

The TGA and differential thermogravimetric analysis (DTG) curves for ferritin are shown in Fig. 3.2. Initial mass loss around 100 ^{o}C can be attributed to loss of surface adsorbed water. After this, the rapid mass loss can be attributed to decomposition of protein shell of ferritin. Protein molecules are known to decompose between 150 and 300 ^{o}C [92]. The mass loss at 420 ^{o}C must represent decomposition of ferritin cores. The mass of sample becomes almost constant around 550 ^{o}C. Two major mass losses around 800 and 970 ^{o}C are again observed. Mass of the system becomes almost constant after this temperature.

The ferritin is heated in air for three hours at 100, 200 and 300 ^{o}C. The x-ray diffraction patterns of these samples are almost similar to that of original sample. That is, the core of ferritin does not yet start to decompose. In other words, only protein shell of ferritin has decomposed by this temperature. The resulting sample is

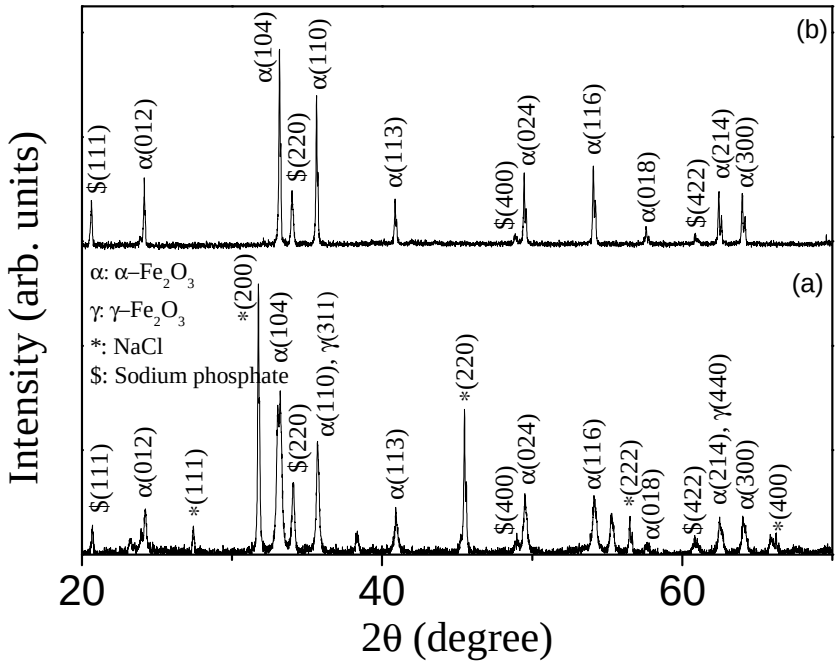

Fig. 3.3: X-ray diffraction patterns of ferritin samples heated at (a) 550 and (b) 1050 ^{o}C.

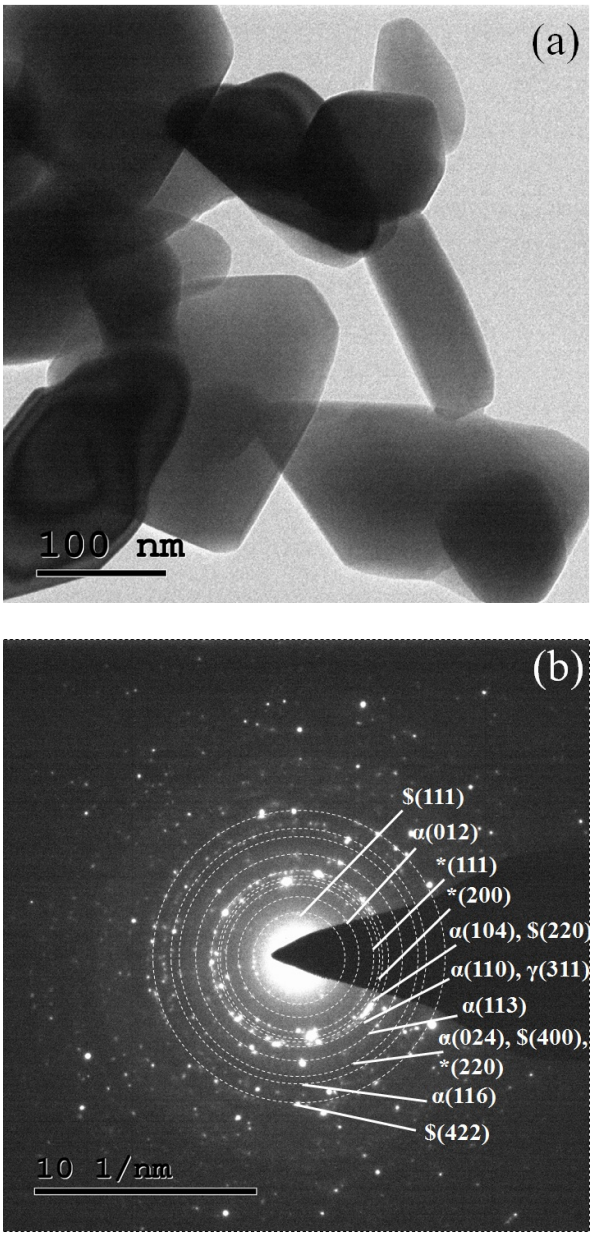

Fig. 3.4: (a) Transmission electron micrograph and (b) selected area electron diffraction pattern for ferritin sample heated at 550 ^{o}C. Dotted circles are visual guides.

again heated in air at 550 ^{o}C for three hours. X-ray diffraction pattern of this sample is shown in Fig. 3.3 (a). This heat treated sample contains a mixture of γ-Fe_2O_3, α-Fe_2O_3, NaCl and sodium phosphate [93–96]. The sodium phosphate must be formed due to the reaction between phosphate and sodium ions. One group reported formation of sodium sulfate due to heat treatment of ferritin [78]. Formation of iron oxide nanoparticles

by heating monolayer and multilayer of horse spleen ferritin at 400 ^{o}C has also been reported [78]. It is claimed that monolayer results only γ-Fe_2O_3 whereas multilayers results a mixture of γ-Fe_2O_3 and α-Fe_2O_3 phases. Origin of mass loss around 800 ^{o}C is very interesting. It is melting point of NaCl. Usually, melting process does not cause any mass loss. But NaCl has an interesting characteristic behaviour. The NaCl releases

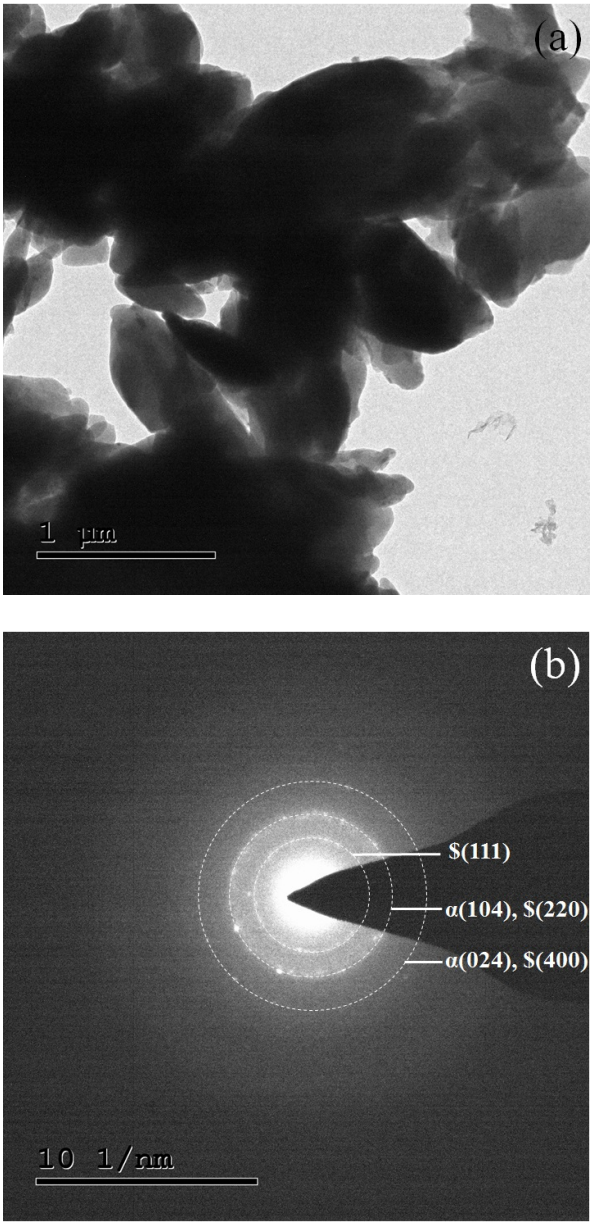

Fig. 3.5: (a) Transmission electron micrograph and (b) selected area electron diffraction pattern for ferritin sample heated at 1050 ^{o}C. Dotted circles are visual guides.

chlorine gas after melting and reacts with atmospheric oxygen to form Na_2O followed by formation of Na_2O_2 [97–100]. Melting point of Na_2O_2 is 495 ^oC and so vaporizes immediately [101]. In this way, NaCl is eliminated from the system. This whole process begins around 800 ^oC and completes by 1035 ^oC. The decomposed ferritin sample is heated at 1050 ^oC for three hours in air. The x-ray diffraction pattern of this sample is shown in Fig. 3.3 (b). This final sample is seen to consist of only α-Fe_2O_3 and sodium phosphate. Somewhere beyond 550 ^oC, γ-Fe_2O_3 converts in to α-Fe_2O_3. This conversion does not involve any change in mass of system. Bulk γ-Fe_2O_3 converts to α-Fe_2O_3 between 400 and 600 ^oC [102, 103]. This transition temperature is affected by several factors such as particle size, lattice defects, pressure, method of synthesis, dopants etc [104, 105]. The transition has also been found to occur at 750 ^oC for γ-Fe_2O_3 nanoparticles synthesized using NaOH. It is claimed that sodium ions diffuse in the lattice of γ phase and hence hinder the process [105]. Recently, we studied thermal decomposition of two and six lines ferrihydrite nanoparticles [73]. It is found that both samples decompose to α-Fe_2O_3 on heating in air above 440 ^oC. The decomposition of two and six lines ferrihydrite are also seen to be quite sharp. It is observed in present study that decompositions of ferrihydrite and ferritin are not similar.

Both heated samples are further characterized with transmission electron microscope. For this, one drop of dispersion of powder sample in ethanol is allowed to dry on carbon coated copper grid. Figures 3.4 (a) and 3.5 (a) show transmission electron micrographs of samples. These micrographs show that the particle size increases with increasing temperature of heat treatment. Selected area electron diffraction patterns from both samples are also recorded to detect any presence of other iron oxide phases. Figures 3.4 (b) and 3.5 (b) show selected area electron diffraction patterns. Origin of each ring is also indexed. In Fig. 3.4 (b), electron diffraction from γ-Fe_2O_3, α-Fe_2O_3, NaCl and sodium phosphate are clearly seen whereas in Fig. 3.5 (b) diffraction from α-Fe_2O_3 and sodium phosphate are visible.

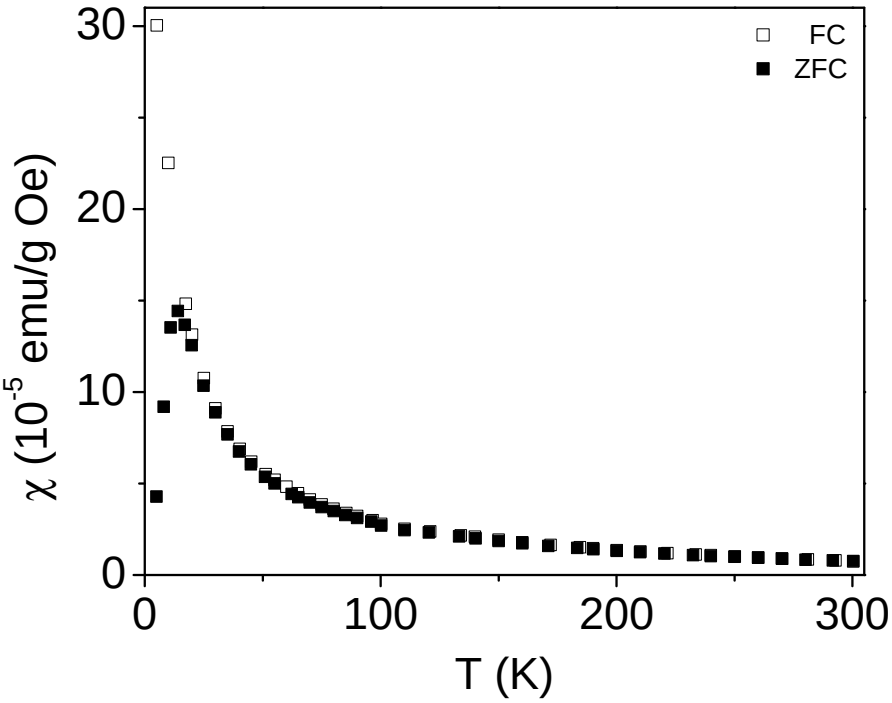

Fig. 3.6: ZFC (solid symbol) and FC (open symbol) susceptibility χ as a function of temperature T for ferritin in 250 G applied magnetic field.

3.2 Magnetization

3.2.1 Temperature dependence

Figure 3.6 shows zero field cooled (ZFC) and field cooled (FC) susceptibility χ as a function of temperature T in 250 G applied magnetic field for ferritin. This figure shows that the ZFC and FC curves bifurcate at temperature $T_{bf} \approx 17$ K. A peak is also seen in the ZFC curve near this temperature. However, the FC susceptibility is seen to decrease monotonically with increasing temperature. These are characteristics of a superparamagnetic system.

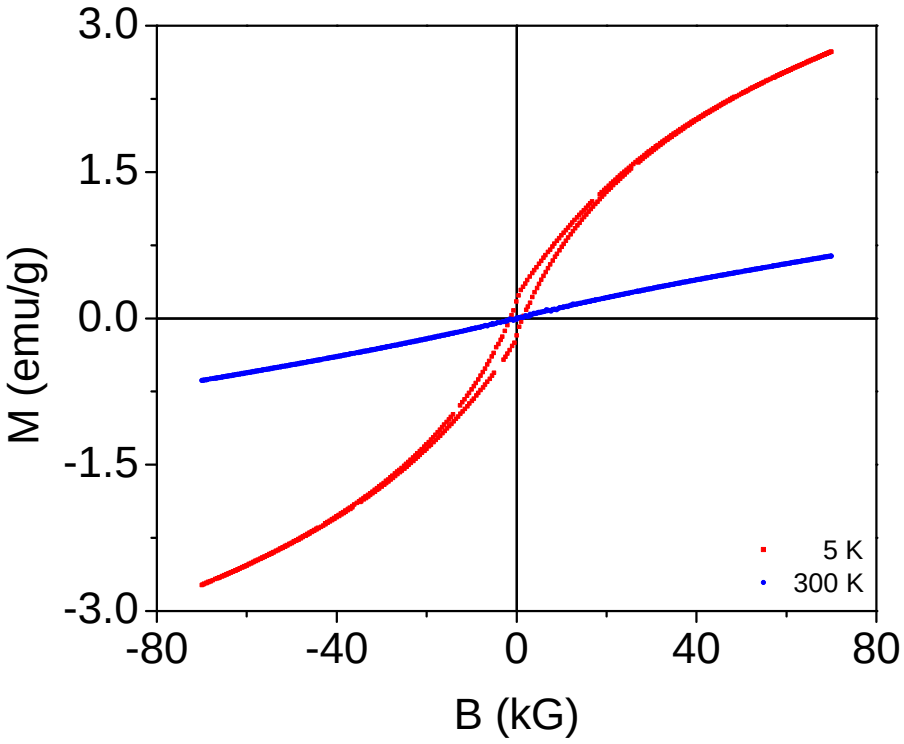

Fig. 3.7: M-B loops for ferritin at 5 and 300 K.

3.2.2 Field dependence

Figure 3.7 shows M-B loops at 5 and 300 K. The data at 5 K shows a hysteresis. This temperature is below the bifurcation temperature T_{bf}. In this region, the magnetization relaxes slowly and a hysteresis in the M-B loop is seen. The system is in superparamagnetic state above the bifurcation temperature T_{bf}. The magnetization relaxation is extremely fast in this region and so any hysteresis is not seen in the M-B loop. Because of this reason, there is no hysteresis at 300 K.

Figure 3.8 shows magnetization M as a function of applied magnetic field B for ferritin at different temperatures in superparamagnetic region. The magnetization increases with increasing strength of applied magnetic field. At higher magnetic fields, specially, the magnetization increases almost linearly with applied field. The magnetization is also seen to decrease with increasing temperature. These observations are

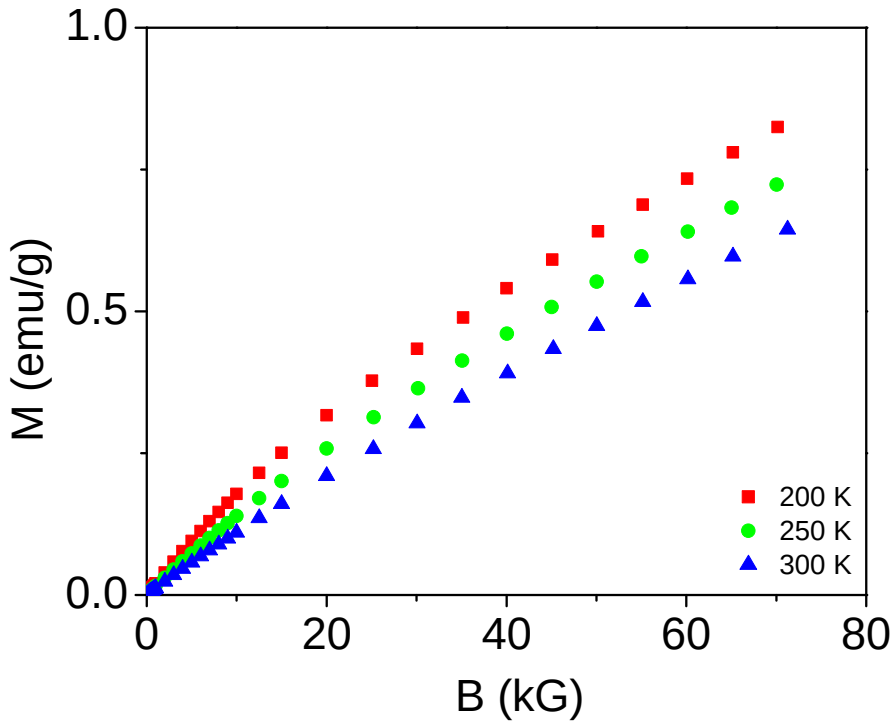

Fig. 3.8: Magnetization M as a function of applied magnetic field B for ferritin at different temperatures.

as per expectation for antiferromagnetic nanoparticle systems in superparamagnetic region.

3.3 Particle Size Distribution

Magnetization M of antiferromagnetic particles, in superparamagnetic state, as function of applied magnetic field B and temperature T is described as [41–45, 47, 48, 50–52, 106]

$$M = M_0 L(x) + \chi B, \tag{3.1}$$

where $L(x) = [\coth(x) - (\frac{1}{x})]$ is the Langevin function and $x = \frac{\mu B}{k_B T}$. Here M_0 is saturation magnetization, μ is particle magnetic moment, k_B is the Boltzmann constant and χ is antiferromagnetic susceptibility of particle core. Particle magnetic moment in

antiferromagnetic particles arises due to presence of uncompensated spins on surface [80], whereas the core does not have any contribution. If it is assumed that these spins appear randomly then there will be about $\sqrt{N_s}$ uncompensated spins on the surface, where N_s is number of spins in the particle. In other words, the particle magnetic moment of antiferromagnetic nanoparticle is directly proportional to square root of particle volume V. That is, for spherical particles such as ferritin $\mu(D) = CD^{3/2}$. Here C is a material dependent constant. Value of this constant can be calculated if crystal structure of the material is correctly known. Here, this calculation is avoided for ferritin because of its still disputed crystal structure [65].

The distribution of particle size in a nanoparticle system can be described by a

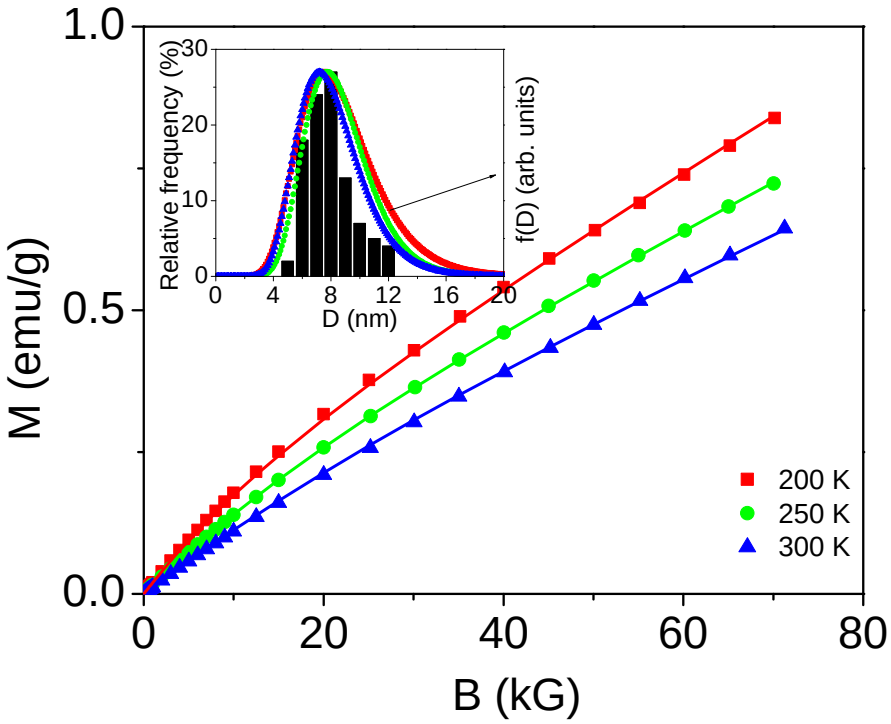

Fig. 3.9: Magnetization M as a function of applied magnetic field B for ferritin at different temperatures. Solid lines show fit to Eq. (3.3). Inset shows histogram for particle size distribution. Curves show estimated particle size distribution.

Tab. 3.1: Values of fit parameters N,C, s, n, and χ to Eq. (3.3) and the values of R^2 for ferritin at different temperatures.

T (K)	N (10^{16} /g)	C ($\mathrm{nm}^{-3/2}$)	s	n (nm)	$\chi(10^{-6}$ emu/g Oe)	R^2
200	6.85	12.30	0.295	8.20	9.27	0.9991
250	6.68	12.31	0.299	8.06	8.03	0.99997
300	6.32	12.20	0.256	7.90	7.13	0.9998

log-normal distribution function [48, 51, 107]

$$f(D) = \frac{1}{Ds\sqrt{2\pi}} \exp(-\frac{[\ln(\frac{D}{n})]^2}{2s^2}), \tag{3.2}$$

where s and n are parameters characterizing the distribution. Considering this distribution in particle size, Eq. (3.1) takes the form

$$M(B,T) = N \int_0^\infty \mu(D)L(x)f(D)dD + \chi B, \tag{3.3}$$

where N is total number of particles contributing to magnetization. This equation is used to fit magnetization as a function of applied magnetic field data, shown in Fig. 3.8, for ferritin. A non linear least square fit procedure is followed. Required computer codes are written in Python. Estimated values of parameters N, C, s, n and χ are shown in Table 3.1. Coefficient of determination R^2, a measure of goodness of fit, is also shown in the table. The resulting fits are shown as solid lines in Fig. 3.9. The quality of fit is seen to be good. The estimated particle size distribution is shown in the inset. It is very much clear that the estimated particle size distribution matches reasonably well with that determined from transmission electron micrograph.

3.4 Magnetic Anisotropy

While deriving Eq. (3.3), it is assumed that there is no anisotropy in the system. But, this assumption is not true. In superparamagnetic region, the magnetic anisotropy energy is smaller than the thermal energy. For uniaxial system [5], the magnetocrystalline anisotropy energy is approximately equal to $-KV\cos^2\beta$, where β is angle between particle magnetic moment $\vec{\mu}$ and easy axis $\vec{e}$. Here K is anisotropy constant and V is particle volume. In presence of external magnetic field B, energy E of a particle is sum of Zeeman energy and magnetocrystalline anisotropy energy. That is,

$$E(\alpha,\beta) = -\mu B\cos\alpha - KV\cos^2\beta, \tag{3.4}$$

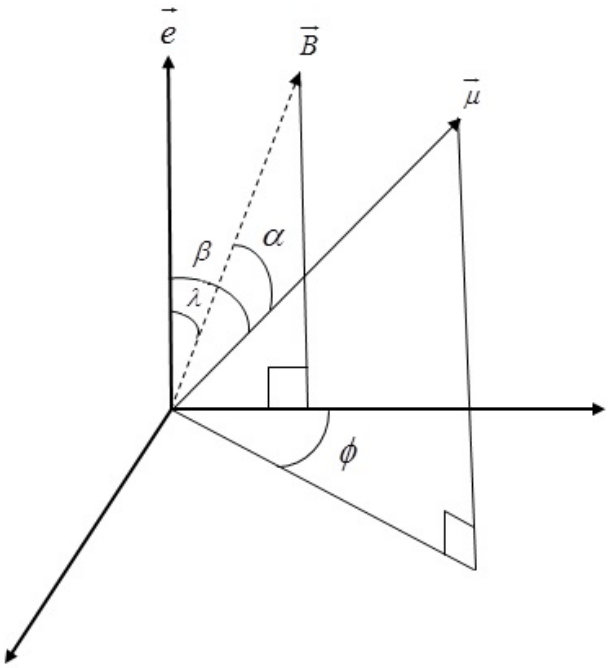

Fig. 3.10: Angles α, β, λ and ϕ used in calculation of magnetization.

where α is angle between magnetic moment $\vec{\mu}$ and applied magnetic field $\vec{B}$. Using Boltzmann statistics and theory of canonical ensemble, the mean value of projection of $\vec{\mu}$ along the applied magnetic field direction [108]

$$\bar{\mu} = \frac{\int_0^{2\pi}\int_0^{\pi} \mu \cos\alpha \exp(-\frac{E(\alpha,\beta)}{k_B T}) \sin\beta d\beta d\phi}{\int_0^{2\pi}\int_0^{\pi} \exp(-\frac{E(\alpha,\beta)}{k_B T}) \sin\beta d\beta d\phi}, \tag{3.5}$$

where various angles are shown in Fig. 3.10 and related as $\cos\alpha = \sin\lambda \sin\beta \cos\phi + \cos\lambda \cos\beta$. Equation (3.5) can be written as

$$\bar{\mu}(\lambda) = \mu \frac{T(\lambda)}{N(\lambda)}, \tag{3.6}$$

where

$$T(\lambda) = \int_0^{2\pi}\int_0^{\pi} [\sin\lambda \sin\beta \cos\phi + \cos\lambda \cos\beta] \exp(-\frac{E(\alpha,\beta)}{k_B T}) \sin\beta d\beta d\phi \tag{3.7}$$

and

$$N(\lambda) = \int_0^{2\pi}\int_0^{\pi} \exp(-\frac{E(\alpha,\beta)}{k_B T}) \sin\beta d\beta d\phi. \tag{3.8}$$

$T(\lambda)$ and $N(\lambda)$ can be further simplified and written in terms of modified Bessel's functions [58]. However in this work, Eqs. (3.7) and (3.8) are used as such. In a sample of magnetic nanoparticles, the anisotropy axes of N particles are randomly oriented and so the expression for magnetization of the system

$$M = \frac{N}{4\pi} \int_0^{2\pi} d\phi \int_0^{\pi} \bar{\mu}(\lambda) \sin\lambda d\lambda = \frac{N\mu}{2} \int_0^{\pi} \frac{T(\lambda)}{N(\lambda)} \sin\lambda d\lambda. \tag{3.9}$$

Here saturation magnetization of the system $M_0 = N\mu$. This expression for magnetization assumes that all particles have equal volume. But, this assumption is not true

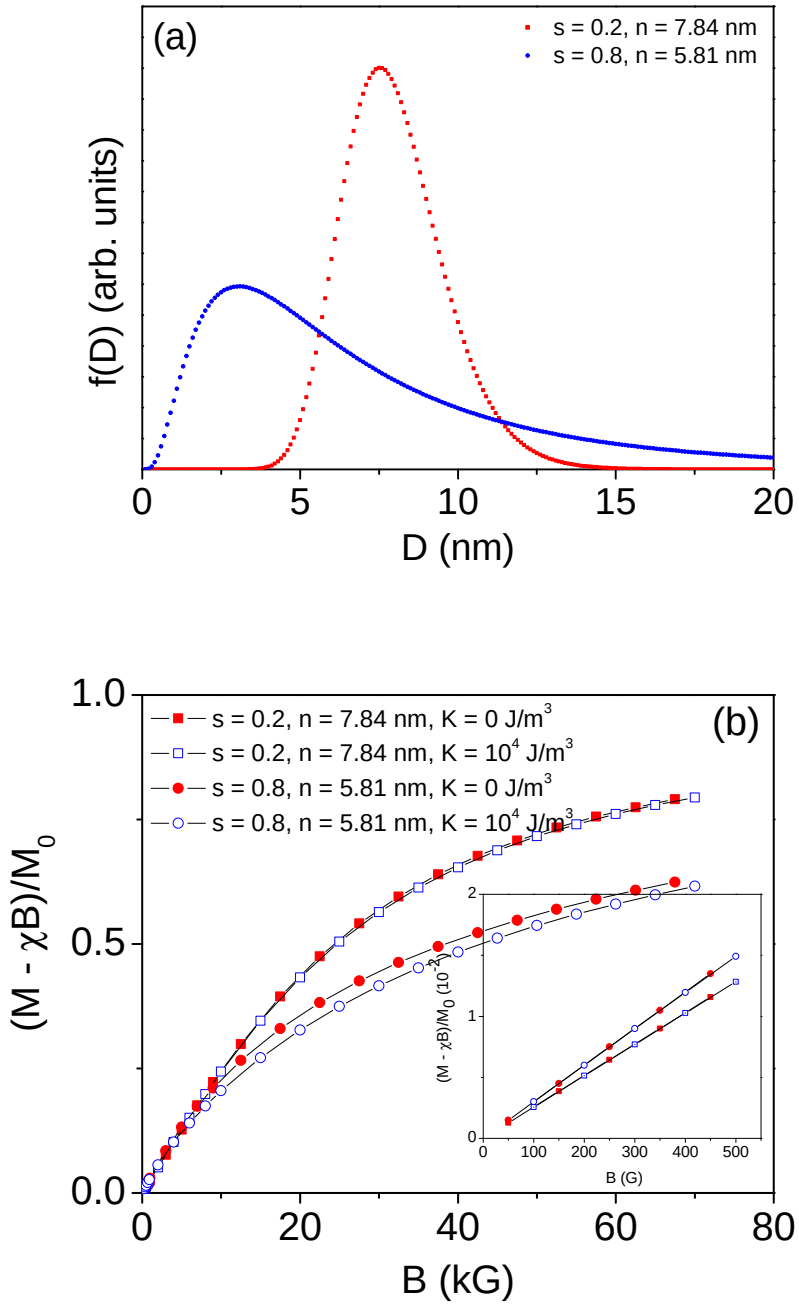

Fig. 3.11: (a) Log-normal distribution in particle diameter for two different values of parameters s and n and (b) calculated magnetization curves for corresponding particle size distributions considering absence (solid symbols) and presence (open symbol) of magnetic anisotropy at 250 K.

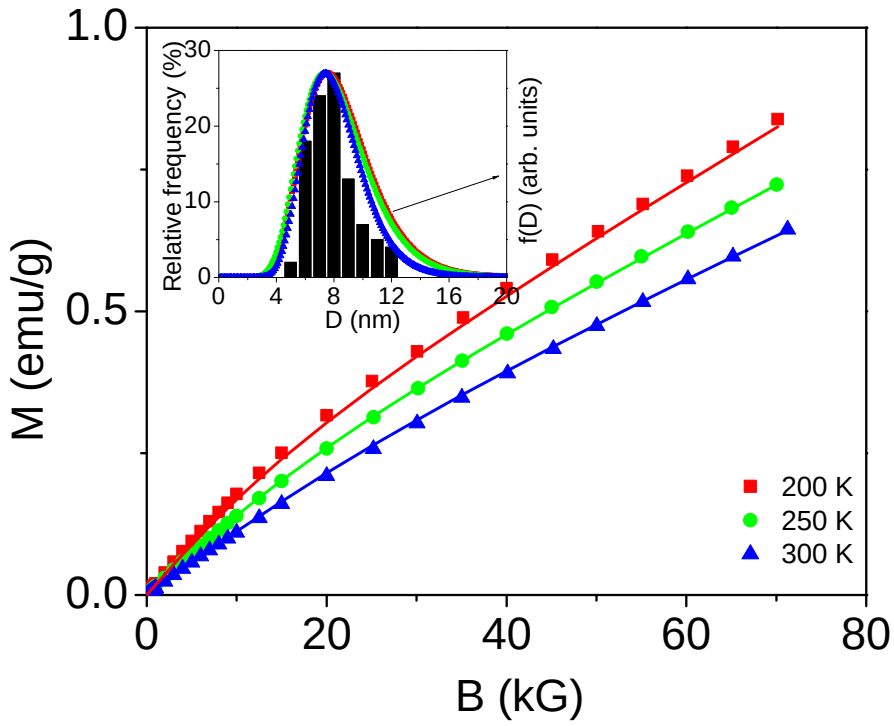

Fig. 3.12: Magnetization M as a function of applied magnetic field B for ferritin at different temperatures. Solid lines show fit to Eq. (3.11). Inset shows histogram for particle size distribution. Curves show estimated particle size distribution.

for a real sample of nanoparticles. There is always a distribution in particle volume due to distribution in particle size and shape. For spherical particles $V(D) = \frac{\pi}{6}D^3$. The distribution in particle diameter D can be described by Eq. (3.2). Considering this distribution, the expression for magnetization takes form

$$M(B,T) = \int_0^\infty Mf(D)dD, \tag{3.10}$$

where M is given by Eq. (3.9). This equation describes the magnetization of ferro and ferrimagnetic nanoparticles. The magnetization of antiferromagnetic nanoparticles will be described by

$$M(B,T) = \int_0^\infty Mf(D)dD + \chi B. \tag{3.11}$$

Tab. 3.2: Values of fit parameters N,C, K, s, n, and χ to Eq. (3.11) and the values of R^2 for ferritin at different temperatures.

T (K)	N (10^{16} /g)	C ($\mathrm{nm}^{-3/2}$)	K (10^4 Jm^{-3})	s	n (nm)	χ(10^{-6} emu/g Oe)	R^2
200	7.20	12.41	1.75	0.320	8.34	9.30	0.9998
250	6.78	12.36	1.59	0.267	8.32	8.00	0.99999
300	6.25	12.26	1.50	0.285	7.80	7.16	0.99992

From Eq. (3.11), after subtracting the linear term in B from magnetization $M(B,T)$ and normalizing it by saturation magnetization $M_0 = N\mu$, one finds that a plot of $(M-\chi_a B)/M_0$ as a function of B at a given temperature T only depends on parameters C, K, s and n. In other words, this plot should explain the magnetization process going on inside the system. Figure 3.11 (a) shows plots of two log-normal distributions for particle diameter. The curve corresponding to $s = 0.2$ represents a narrow distribution whereas the curve corresponding to $s = 0.8$ represents a wide distribution. The value of parameter n is chosen in such a way that the mean particle diameter, which is $n\sqrt{e^{s^2}}$, is 8 nm. The magnetization curve is calculated for these two distributions considering the absence and presence of magnetic anisotropy at 250 K using Eq. (3.11). The data are shown in Fig. 3.11 (b). Interesting observations are made from these plots. The magnetization is greatly affected by the particle size distribution at lower as well as higher magnetic fields. The same is seen to be affected by magnetic anisotropy only at higher magnetic fields. The difference is seen to be small for narrow particle size distribution. It is also worth mentioning here that Eq. (3.11) takes form of Eq. (3.3) if $K = 0$.

From Eq. (3.11), it is clear that the magnetization of antiferromagnetic nanoparticle systems in superparamagnetic region depends on parameters N, C, K, s, n and χ. Values of these parameters are estimated for ferritin by fitting the M versus B data shown in Fig. 3.8 to Eq. (3.11). This fit involves rigorous and time consuming calcu-

lations. This process is speeded up by using several processors working in parallel. Fit parameters are finalized after 10^4 iterations. The estimated values of parameters are shown in Table 3.2. These new sets of parameters are seen to differ only slightly from those shown in Table 3.1 because of narrow particle size distribution in ferritin. It is worth mentioning here that bulk form of ferritin does not exist. Anisotropy constant of any material is affected by presence or absence of factors like stress and strain [109–111]. It is also found to be dependent on particle size [112]. The resulting fits are shown in Fig. 3.12 as solid lines. The inset shows estimated particle size distribution. A slight improvement in quality of fit is evident from increased R^2 values. One can still get slightly better fit parameters by using much faster computational facility.

3.5 Conclusion

In this Chapter, detailed investigations on structural, thermal and magnetic characterization ferritin nanoparticles are reported. The cores of ferritin are 8 nm in size and poorly crystalline. These inorganic cores contain 10 wt% iron. Ferritin cores are stable up to 300 ^{o}C. The cores decompose to a mixture of γ-Fe_2O_3 and α-Fe_2O_3 on heating in air at 550 ^{o}C. This mixture stabilizes to α-Fe_2O_3 on further heating in air at 1050 ^{o}C. The ferritin cores are found to be antiferromagnetic in nature. Both particle size distribution and magnetic anisotropy affect the magnetization of superparamagnetic systems. Values of different fit parameters are estimated by fitting the magnetization as a function of applied magnetic field data to appropriate expressions. This work also provides an easy and convenient method to estimate particle size distribution present in magnetic nanoparticle systems.

Chapter 4

NICKEL OXIDE NANOPARTICLES

In this chapter preparation, structural and magnetic characterization of NiO nanoparticles are discussed.

4.1 Structural Characterization

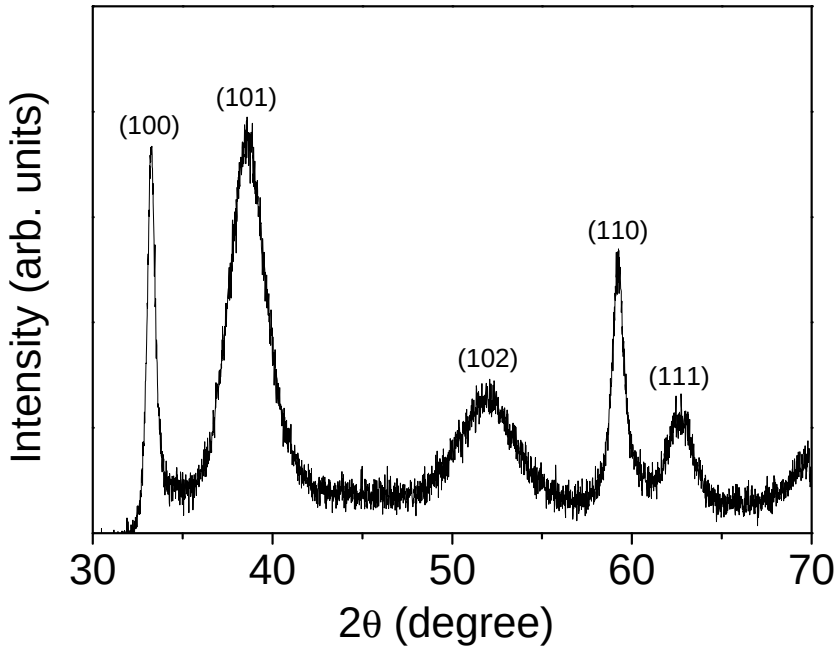

Fig. 4.1: X-ray diffraction pattern of β-Ni$(OH)_2$ powder sample.

This chapter is based on following published work:
Role of wide particle size distribution on magnetization, Navneet Kaur and S. D. Tiwari, Applied Physics A: Materials Science & Processing **126**, 349 (2020).

X-ray diffraction pattern of synthesized green coloured powder sample is shown in Fig. 4.1. This pattern confirms that the sample is single phase hexagonal β-$Ni(OH)_2$ [83]. Thermal decomposition of this material is studied with thermogravi-

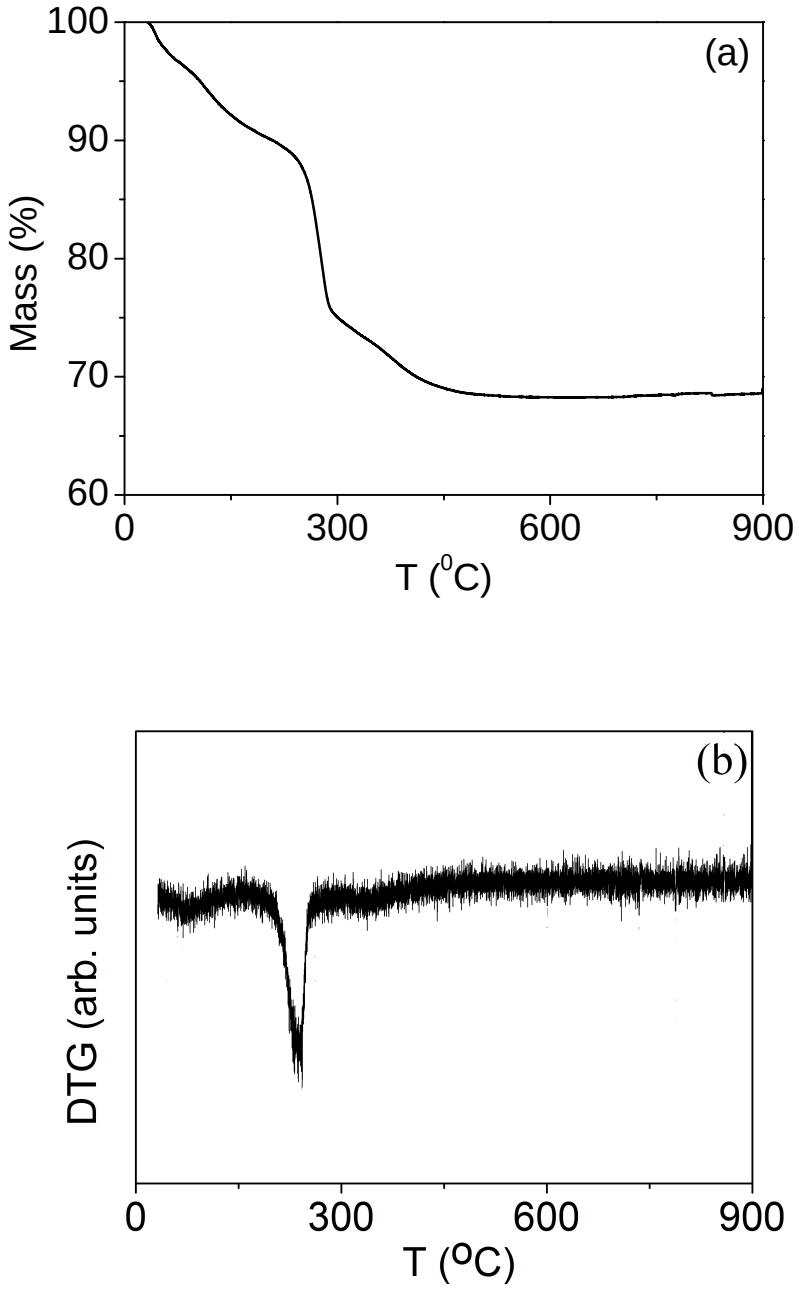

Fig. 4.2: (a) TGA and (b) DTG curves for β-$Ni(OH)_2$.

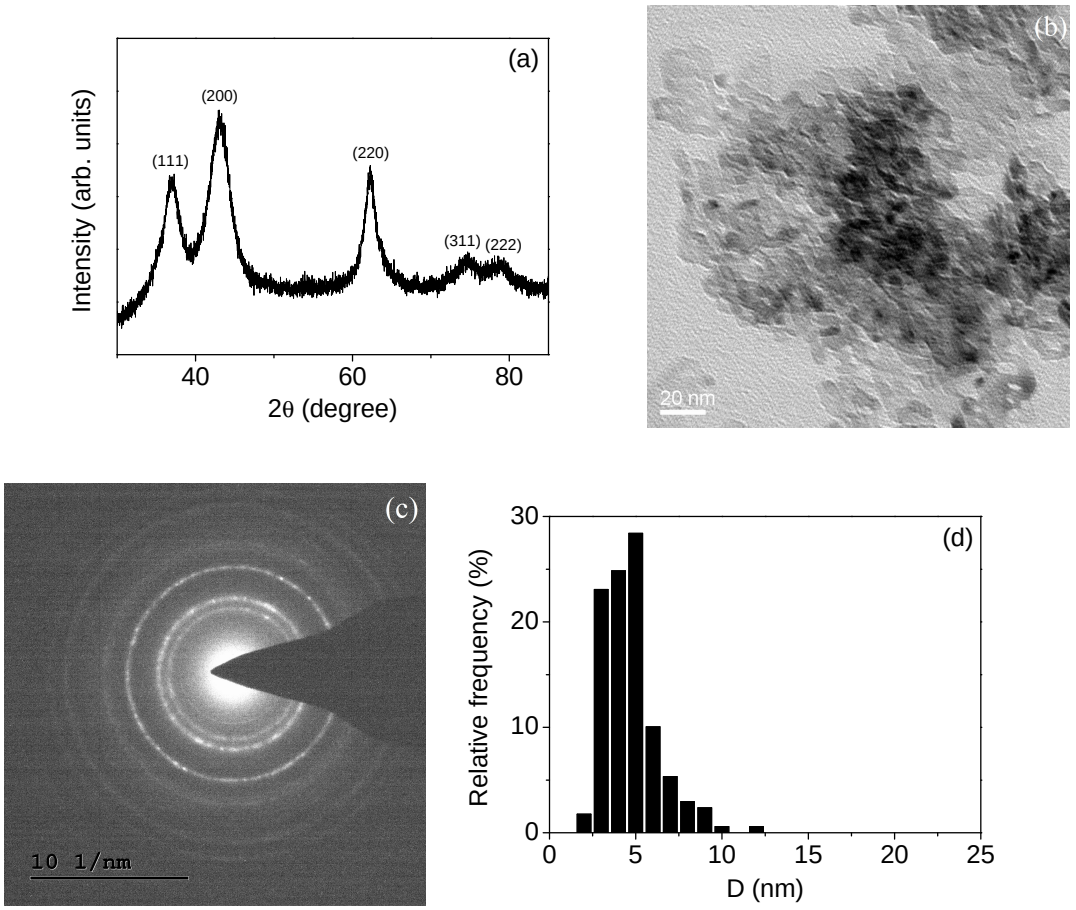

Fig. 4.3: (a) Room temperature x-ray diffraction pattern, (b) transmission electron micrograph, (c) selected area electron diffraction pattern and (d) a histogram of the distribution of particle sizes for NiO sample prepared by heating β-$Ni(OH)_2$ at 250 ^{o}C.

metric analyzer (TGA). For this, the sample is heated in air at constant heating rate of 5 ^{o}C per minute. The TGA and differential thermogravimetric analysis (DTG) curves for β-$Ni(OH)_2$ are shown in Fig. 4.2. Initial mass loss around 100 ^{o}C can be attributed to loss of surface adsorbed water. The mass loss at 250 ^{o}C must represent decomposition of the sample. Mass of the system becomes almost constant after this temperature. The x-ray diffraction pattern of this decomposed sample confirms that β-$Ni(OH)_2$ decomposes to NiO on heating in air above 250 ^{o}C.

Two samples of NiO are prepared by heating β-$Ni(OH)_2$ at 250 and 300 ^{o}C for

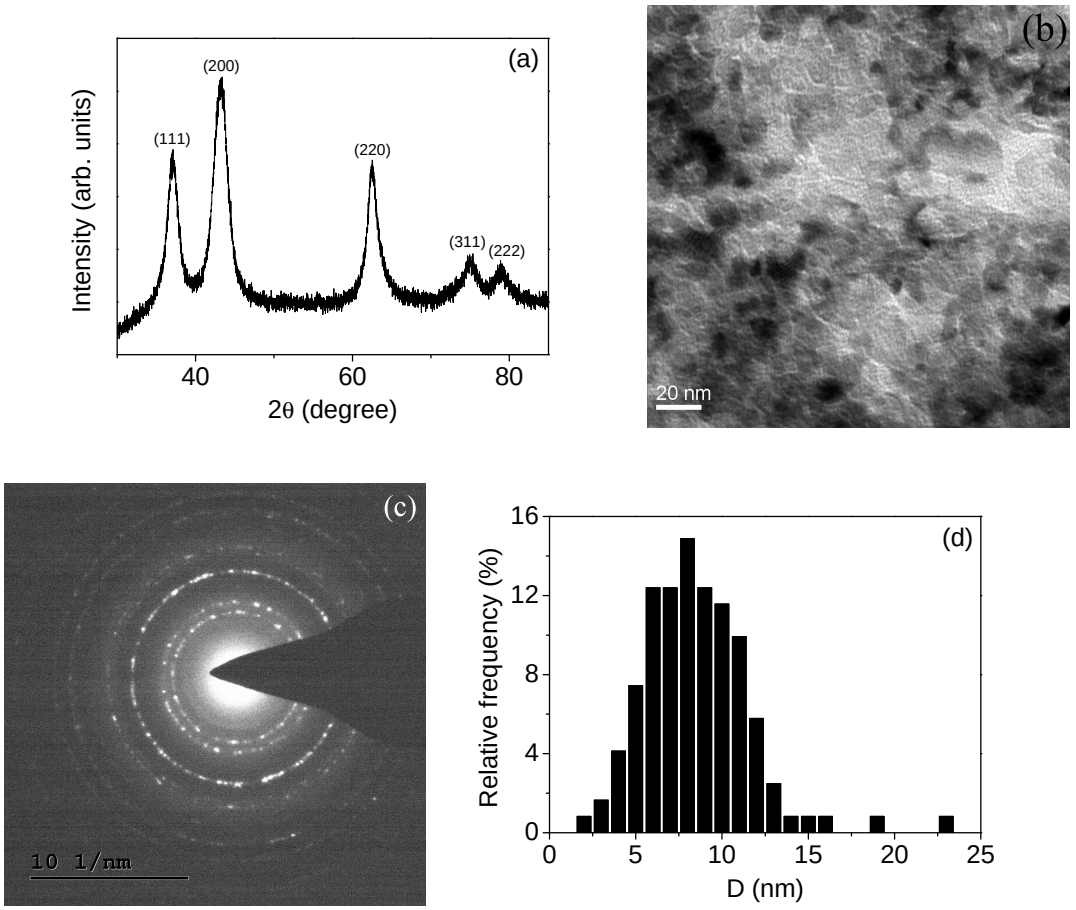

Fig. 4.4: (a) Room temperature x-ray diffraction pattern, (b) transmission electron micrograph, (c) selected area electron diffraction pattern and (d) a histogram of the distribution of particle sizes for NiO sample prepared by heating β-$Ni(OH)_2$ at 300 ^{o}C.

three hours in inert atmosphere. Room temperature x-ray diffraction patterns of these samples are shown in Figs. 4.3 (a) and 4.4 (a). These patterns confirm that the samples are single phase FCC NiO [82]. The diffraction peaks are seen to be very broad. It indicates that samples are nanocrystalline. The average crystallite size is calculated using the modified Scherrer formula [86]

$$t = \frac{K\lambda}{\cos\theta_B(B_M - B_S)} \tag{4.1}$$

where λ is the wavelength of the x-ray, θ_B is the Bragg angle, B_M is the full width at

half maximum of a peak and B_S is the full width at half maximum of the same peak of a standard sample. Bulk NiO powder is used as the standard. Value of K depends on shape of particles. Three most intense peaks are used to calculate the average crystallite size which turn out to be 5 and 8 nm considering $K = 0.9$. Instrumental broadening is taken care in calculation by using $(B_M - B_S)$ instead of B_M in the formula. Figures 4.3 (b) and 4.4 (b) show transmission electron micrographs of NiO samples. Particles are seen to be of different shapes and sizes. Selected area electron diffraction patterns are shown in Figs. 4.3 (c) and 4.4 (c). Rings in these patterns once again confirm the crystalline nature of samples. Particle size distributions are determined using transmission electron micrographs. These distributions are based on size measurement of 100 particles and shown in Figs. 4.3 (d) and 4.4 (d). Histograms are seen to peak at 5 and 8 nm.

4.2 Magnetization

4.2.1 Temperature dependence

Figure 4.5 shows zero field cooling (ZFC) and field cooling (FC) susceptibility χ as a function of temperature T in presence of 250 G external applied magnetic field. Bifurcation of ZFC and FC curves are clearly visible. A nanoparticle system remains in superparamagnetic state above this bifurcation temperature.

4.2.2 Field dependence

Figure 4.6 shows M-B loops for 5 and 8 nm NiO particles at 10 and 350 K. At low temperature, the particle magnetic moments get blocked and so relax slowly. Due to this, a hysteresis is seen in the M-B loop at 10 K. Above the bifurcation temperature, the particle magnetic moments flip very fast and there is no hysteresis in the M-B loop at 350 K. Magnetization M as a function of applied magnetic field B data at 350

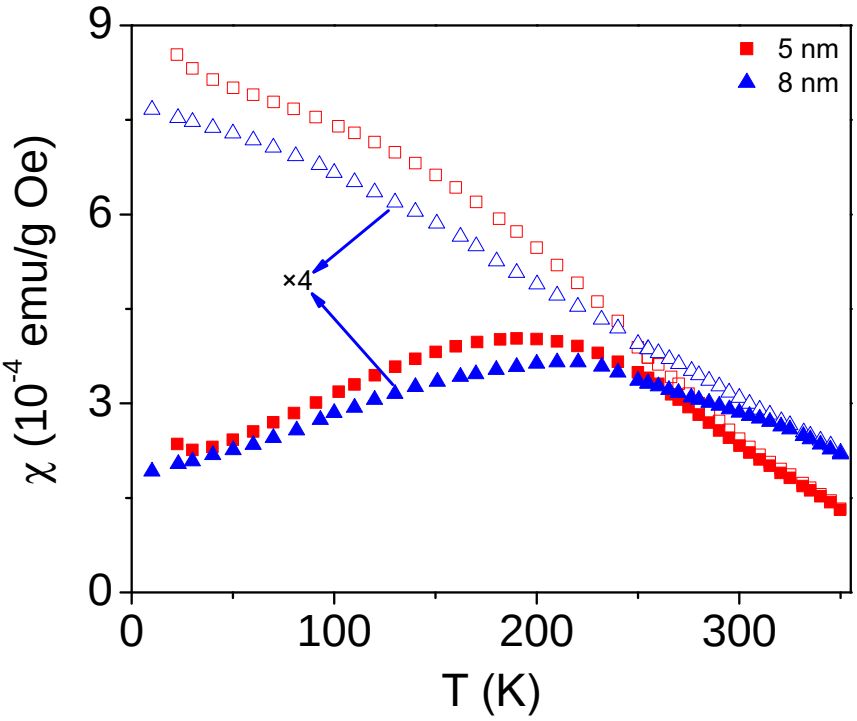

Fig. 4.5: ZFC (solid symbol) and FC (open symbol) susceptibility χ as a function of temperature T for 5 and 8 nm NiO particles in 250 G applied magnetic field.

K for 5 and 8 nm NiO particles are shown in Fig. 4.7. The magnetization is seen to increase with increasing strength of applied magnetic field. It is seen to vary almost linearly at higher magnetic fields. Magnetization of 5 nm sample is higher than that of 8 nm sample because the fraction of spins lying on the surface increases with decreasing particle size.

4.3 Particle Size Distribution

Néel proposed models for the origin of particle magnetic moment in NiO particles [80]. If a particle consists of N' spins then there will be approximately $\sqrt{N'}$ uncompensated spins on the surface. NiO has fcc crystal structure with lattice constant 4.176 Å. Assuming that particles are spherical and moment of each Ni^{2+} ion is 2 μ_B [81], the

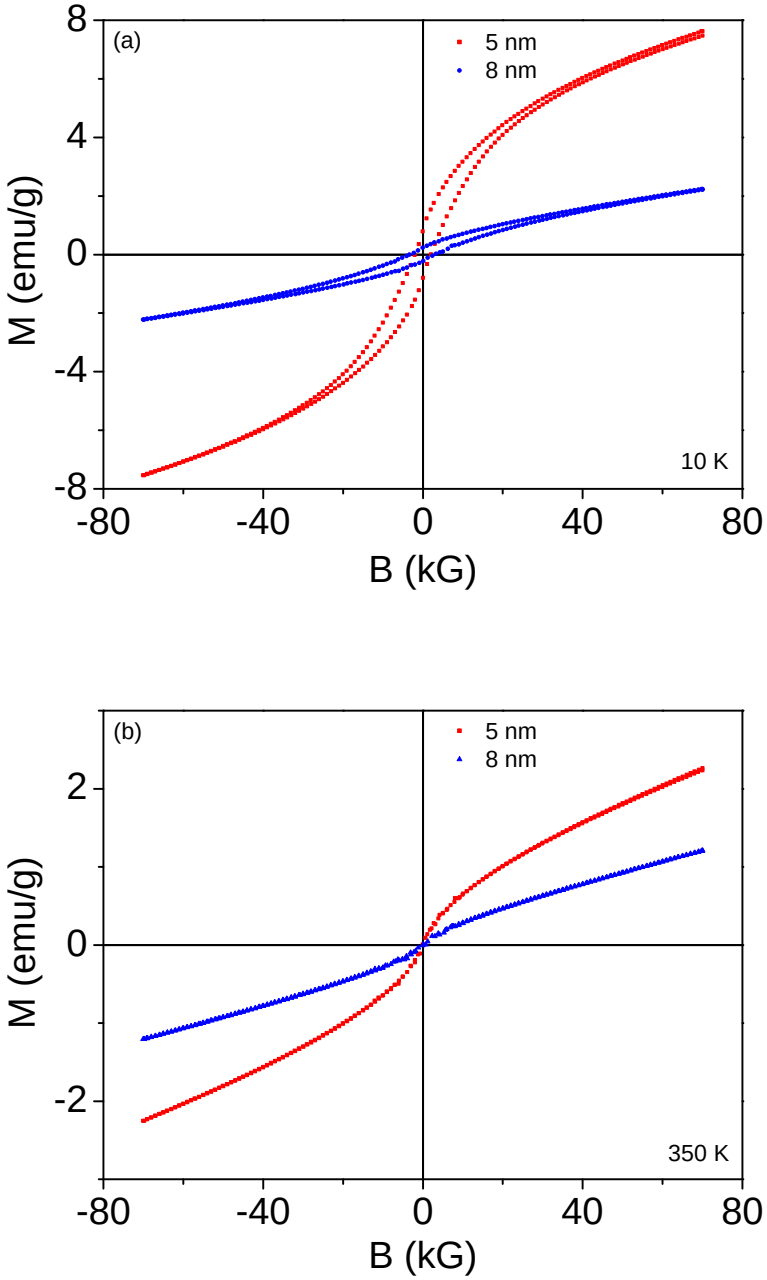

Fig. 4.6: M-B loops for 5 and 8 nm NiO particles at two different temperatures.

particle magnetic moment of a particle of diameter D will be given by relation $\mu(D) = 10.72D^{\frac{3}{2}}$, where D is particle diameter. Considering a log-normal distribution $f(D)$ in

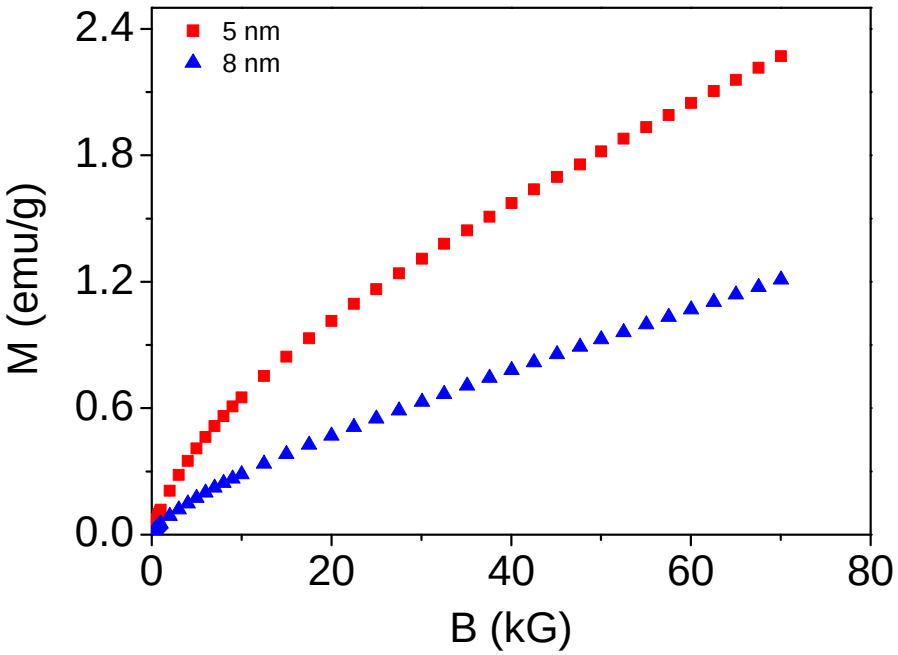

Fig. 4.7: Magnetization M as a function of applied magnetic field B curves for 5 and 8 nm NiO particles at 350 K.

particle size, the expression for magnetization is given by

$$M(B,T) = N \int_0^\infty \mu(D)L(x)f(D)dD + \chi B. \tag{4.2}$$

This equation is used to fit magnetization as a function of applied magnetic field data shown in Fig. 4.7 following a non-linear least square fit procedure. The computer codes are written in Python language. The estimated fit parameters are shown in Table 4.1.

Fitted curves are shown in Fig. 4.8 as solid lines. The fit quality is seen to be good. The estimated particle size distributions are plotted in Fig. 4.9 using values of fit parameters estimated from Table 4.1. This figure compares the estimated particle size distribution with that determined from transmission electron micrograph. The particle size distribution estimated from two independent methods do not match well. The particle size distribution estimated by fitting the magnetization data are found to

Tab. 4.1: Values of fit parameters N, s, n and χ to Eq. (4.2) for NiO samples.

Particle size (nm)	N (10^{17} /g)	s	n (nm)	$\chi(10^{-5}$ emu/g Oe)
5	6.60	0.96	3.45	1.97
8	1.03	0.91	5.41	1.34

be much wider.

In a superparamagnetic system, low field magnetization is governed by particle with larger moments. Contribution of lower moments becomes important at higher fields. In other words, shape of magnetization curve strongly depends on particle size distribution. Anisotropy is another factor affecting the magnetization process. Magnetic anisotropy has several forms [5]. Uniaxial anisotropy is its simplest form. Value of magnetic anisotropy is also reported to depend on particle size [57, 84]. The

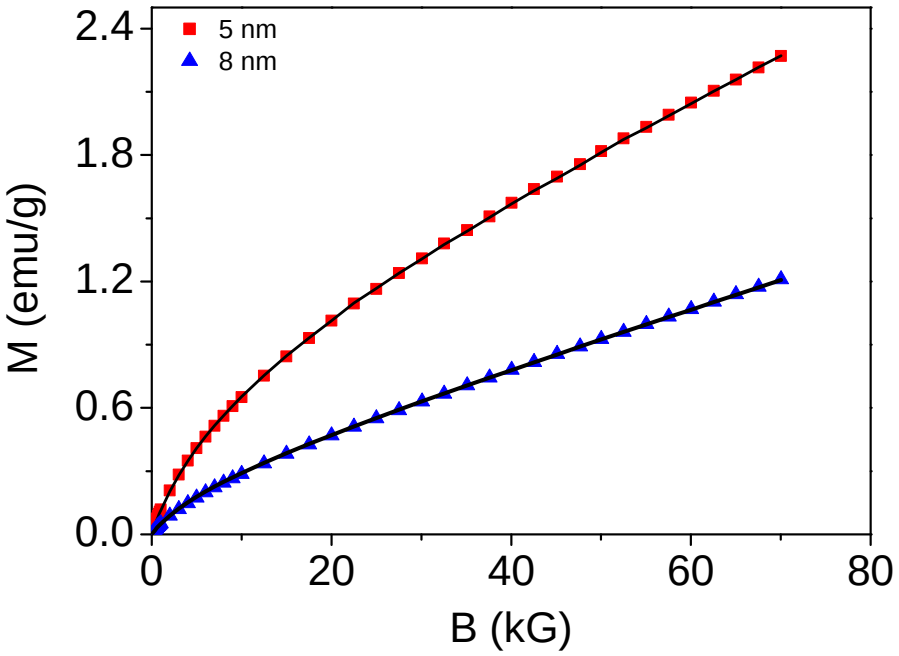

Fig. 4.8: Magnetization M as a function of applied magnetic field B curves for 5 and 8 nm NiO particles at temperature 350 K. Solid lines shows fit to Eq. (4.2)

NiO system has a complicated magnetic anisotropy [113] and so is difficult to consider in present analysis. In Chapter 3, the magnetization curve has been calculated for

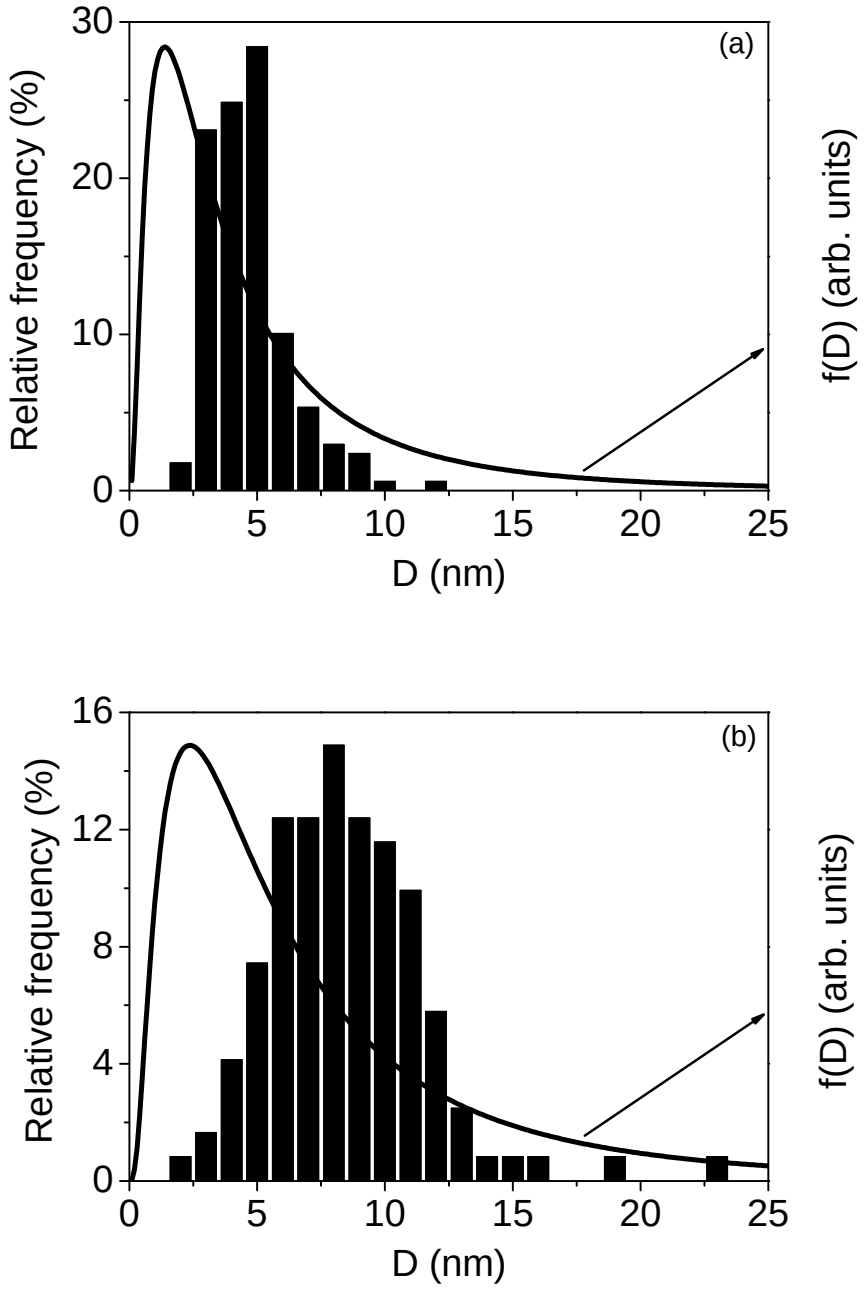

Fig. 4.9: Histogram showing particle size distribution determined from transmission electron micrograph for (a) 5 and (b) 8 nm NiO particles. Solid curves show estimated particle size distribution.

an uniaxial system considering a narrow as well as wide particle size distribution. It was found that both wide particle size distribution and magnetic anisotropy lower the magnetization. Therefore, the particle size distribution in present work is overestimated due to ignorance of magnetic anisotropy.

4.4 Conclusion

In this chapter, a detailed magnetic investigation on 5 and 8 nm NiO particles are discussed. Both samples were found to be superparamagnetic. Magnetization data in superparamagnetic region were analyzed considering a distribution in particle size. The estimated particle size distribution was much wider and did not match well with that determined from transmission electron micrograph. Ignorance of complicated magnetic anisotropy in NiO system while analyzing magnetization data is the reason for this contrary observation.

Chapter 5

CONCLUSIONS

This thesis presents the structural, thermal and magnetic analysis of superparamagnetic Ferritin and NiO nanoparticles. Ferritin is naturally occurring biological system and purchased directly in the form of suspension. On the other hand, two samples of NiO with different particles sizes are synthesized successfully in lab from β-$NiOH_2$. The structural characterization of both samples are done by x-ray diffraction and transmission electron microscope. The x-ray diffraction pattern of ferritin contains broadened humps and sharper peaks. The broadened diffraction humps reveal poorly crystalline nature of ferritin core and sharper peaks belong to NaCl in which ferritin is suspended. X-ray diffraction patterns of NiO samples show broadened diffraction peaks which confirms the nanocrystalline nature of the samples. Average crystallite sizes are calculated from modified Scherrer formula which are found to be 5 and 8 nm. Transmission electron micrograph of ferritin shows inorganic dense cores which are almost spherical in shape. From this micrograph, the histogram is plotted to determine particle size distribution. The average core sizes are found to be *ca.* 8 nm. Transmission electron micrographs of NiO samples show particles are of arbitrary shapes and sizes. The histograms plotted peaks at 5 and 8 nm, indicate the samples have wide particle size distribution. The selected area electron diffraction patterns for both ferritin and NiO nanoparticles show diffractions correspond to x-ray diffraction.

Thermal characterization of ferritin is studied in air using TGA. The DTG curve

shows major mass losses at different temperatures. The mass loss near 100, 200 and 300 ^{o}C are attributed to water loss and denaturation of protein shell. The ferritin core has started decomposing above 420 ^{o}C. In temperature range 790 to 1035 ^{o}C, the mass loss is due to decomposition of NaCl. X-ray diffraction of ferritin heated at 550 ^{o}C contains diffraction lines corresponding to α-Fe_2O_3, γ-Fe_2O_3, NaCl and sodium phosphate. The diffraction pattern of ferritin heated at 1050 ^{o}C shows the presence of α-Fe_2O_3 and sodium phosphate. Selected area diffraction pattern shows rings corresponding to x-ray diffraction peaks. Initially, ferritin cores are supposed to contain major phase ferrihydrite. But, the thermal decomposition of ferritin and ferrihydrite are not alike. Studies claimed that ferrihydrite decompose directly to α-Fe_2O_3 above 440 ^{o}C.

Magnetization measurements of both samples are done using vibrating sample magnetometer. Field cooled and zero field cooled susceptibility curves for ferritin and NiO samples are measured in the presence of 250 G applied field. Field cooled susceptibility curves for samples are observed to be monotonically decreasing with increasing temperature. In case of ferritin, both FC and ZFC curves are seen to bifurcate at 17 K. The peak point in ZFC curve represents the blocking temperature. The bifurcation temperature is almost near to blocking temperature. It is due to narrow particle size distribution of ferritin cores in the sample. Zero field cooled susceptibility curves for 5 and 8 nm samples are seen to bifurcate at 300 and 330 K, respectively. The bifurcation and blocking temperature are far away from each other. It is due to wide particle size distribution.

The M-B loops of ferritin are recorded at 5 and 300 K. A hysteresis has been observed below bifurcation temperature i.e. at 5 K due to slow relaxation of particles. At 300 K, which is far above bifurcation temperature, no hysteresis is observed because with increasing temperature particles starts fluctuating randomly and relaxation rate increases. M-B loops of NiO are measured at 10 and 350 K. At 10 K, M-B loops

exhibit hysteresis but on the other hand at 350 K no hysteresis is observed. These observations clearly show that samples are superparamagnetic above bifurcation temperature. Magnetization as a function of applied magnetic field data are measured at different temperatures for all samples. The magnetization of samples is seen to increase with increasing strength of applied magnetic field and to decrease with increasing temperature. These curves are used to analyse magnetization of the system. These data are fitted to appropriate magnetization expressions considering presence and absence of magnetic anisotropy using a non-linear least square fit procedure. The computer codes are written in python. A log-normal distribution is considered for particle size. The estimation of particle size distribution and that determined from transmission electron micrograph are compared. It is concluded that magnetic anisotropy is more significant in samples with wide particle size distribution. There is minute effect of magnetic anisotropy on magnetization of system of nanoparticles having narrow particle size distribution.

Several types of magnetic anisotropy are found in different magnetic crystals. The uniaxial anisotropy is the simplest type of magnetic anisotropy. Effect of this anisotropy on magnetization has been considered for ferritin. The NiO crystal has somewhat complicated magnetic anisotropy and so its effect on the magnetization process of NiO nanoparticles could not be considered. There are systems having even more complicated form of magnetic anisotropy. In future, one may study effect of particle size distribution and such complicated magnetic anisotropy on magnetization of a collection of nanoparticles.

BIBLIOGRAPHY

[1] B. D. Cullity and C. D. Grahm, *Introduction to Magnetic Materials* (Wiley, New Jersey, 2009).

[2] C. Kittel, *Introduction to Solid State Physics* (Wiley India Pvt. Ltd., New Delhi, 2013).

[3] N. W. Arshcroft and N. D. Mermin, *Solid State Physics* (Cengage Learning India Pvt. Ltd., Delhi, 2017).

[4] A.J. Dekker, *Solid State Physics* (Macmillan Publishers India Ltd., Delhi, 2014).

[5] S. Chikazumi, *Physics of Magnetism* (Wiley, New York, 1964).

[6] J. M. D. Coey, *Magnetism and Magnetic Materials* (Cambridge University Press, New York, 2010).

[7] R. W. Chantrell and K. O'Grady, in *Applied Magnetism*, edited by R. Gerber, C. D. Wright and G. Asti (Kluwer Academic Publishers, The Netherlands, 1994), p. 113.

[8] R. E. Rosensweig, *Ferrohydrodynamics* (Cambridge University Press, Cambridge, 1985).

[9] Q. A. Pankhurst, N. K. T. Thanh, S. K. Jones and J. Dobson, "Progress in Applications of Magnetic Nanoparticles in Biomedicine", J. Phys. D: Appl. Phys. **42**, 224001 (2009).

[10] A. S. Edelstein and R. C. Cammarata, *Nanomaterials: Synthesis, Properties and Applications* (Institute of Physics Publishing, Bristol, 2002).

[11] G. Cao, *Nanostructures and Nanomaterials: Synthesis, Properties and Applications* (Imperial College Press Publishing, London, 2004).

[12] J. N. Tiwari, R. N. Tiwari and K. S. Kim, "Zero - Dimensional, One - Dimensional, Two - Dimensional and Three - Dimensional Nanostructured Materials for Advanced Electrochemical Energy Devices", Progress in Materials Science **57**, 724 (2012).

[13] M. S. Seehra, *Nanostructured Materials: Fabrication to Applications* (Intek Publications, Croatia, 2017).

[14] J. L. Jambor and J. E. Dutrizac, "Occurrence and Constitution of Natural and Synthetic Ferrihydrite, a Widespread Iron Oxyhydroxide", Chem. Rev. **98**, 2549 (1998).

[15] J. G. E. Harris, J. E. Grimaldi, D. D. Awschalom, A. Chiolero and D. Loss, "Excess Spin and the Dynamics of Antiferromagnetic Ferritin", Phys. Rev. B **60**, 3453 (1999).

[16] I. S. Jacobs and C. P. Bean, in *Magnetism*, Vol. III edited by G. T. Rado and H. Suhl (Academic Press Inc., New York, 1963), p. 271.

[17] Q. A. Pankhurst, J. Connolly, S. K. Jones and J. Dobson, "Applications of Magnetic Nanoparticles in Biomedicine", J. Phys. D: Appl. Phys. **36**, R167 (2003).

[18] P. Antoniammal and D. Arivuoli, "Size and Shape Dependence on Melting Temperature of Gallium Nitride Nanoparticles", J. Nanomater. **2012**, ID415797 (2012).

[19] W. A. de Heer, A. Chatelain and D. Ugarte, "A Carbon Nanotube Field - Emission Electron Source", Science **270**, 1179 (1995).

[20] C. Bréchinag, P. Houdy and M. Lahmani, *Nanomaterials and Nanochemistry* (Springer - Verlag Berlin Heidelberg New York, 2007).

[21] C. N. R. Rao, A. Müller and A. K. Cheetham, *The Chemistry of Nanomaterials: Synthesis, Properties and Applications* (Wiley - VCH Verlag GmbH & Co. KGaA, Weinheim, 2004).

[22] X. Luo et al., "Application of Nanoparticles in Electrochemical Sensors and Biosensors", Electroanalysis **18**, 319 (2006).

[23] M. S. Seehra and A. D. Bristow, *Noble and Precious Metals: Properties, Nanoscale Effects and Applications* (Intek Publications, Croatia, 2018).

[24] H. Grabert and M. H. Devoret, *Single Charge Tunneling* (Plenum, New York, 1992).

[25] G. C. Papaefthymiou, "Nanoparticle Magnetism", Nano Today **4**, 438 (2009).

[26] C. P. Poole and F. J. Owens, *Introduction to Nanotechnology* (John Wiley & Sons, New Jersey, 2003).

[27] L. Néel, in *Low Temperature Physics*, edited by C. Dewitt, B. Dreyfus and P. D. de Gennes (Gordan and Beach, New York, 1962), p. 413.

[28] W. F. Brown, Jr., "Thermal Fluctuations of a Single - Domain Particle", Phys. Rev. **130**, 1677 (1963).

[29] D. Fiorani, *Surface Effects in Magnetic Nanoparticles* (Springer US, 2005).

[30] S. D. Tiwari and K. P. Rajeev, "Magnetic Properties of NiO Nanoparticles", Thin Solid Films **505**, 113 (2006).

[31] C. Frandsen, C. W. Ostenfeld, M. Xu, C. S. Jacobsen, L. Keller, K. Lefmann and S. Mørup, "Interparticle Interactions in Composites of Nanoparticles of Ferrimagnetic (gamma - Fe_2O_3) and Antiferromagnetic (CoO, NiO) Materials", Phy. Rev. B **70**, 134416 (2004).

[32] I. J. Bruce and T. Sen, "Surface Modification of Magnetic Nanoparticles with Alkoxysilanes and Their Application in Magnetic Bioseparations", Langmuir **21**, 7029 (2005).

[33] F. Bao, J. L. Yao and R. A. Gu,"Synthesis of Magnetic Fe_2O_3/Au Core/Shell Nanoparticles for Bioseparation and Immunoassay Based on Surface - Enhanced Raman Spectroscopy", Langmuir **25**, 10782 (2009).

[34] R. Hergt, S. Dutz, R. Müller and M. Zeisberger, "Magnetic Particle Hyperthermia: Nanoparticle Magnetism and Materials Development for Cancer Therapy", J. Phys.: Condens. Matter, **18**, S2919 (2006).

[35] J. Estelrich, M. J. Sánchez-Martín and M. A. Busquets, "Nanoparticles in Magnetic Resonance Imaging: From Simple to Dual Contrast Agents", Int. J. Nanomedicine **10**, 1727 (2015).

[36] H. Kang et al., in *Optical Biosensors, second edition* ed. by F. S. Ligler and C. R. Taitt (Elsevier science, USA, 2008) p. 583 - 621.

[37] L. Néel, "Theorie Du Trainage Magnetique Des Ferromagnetiques En Grains Fins Avec Applications Aux Terres Cuites", Ann. Geøphys **5**, 99 (1949).

[38] R. Køtitz, W. Weitschies, L. Trahms and W. Semmler, "Investigation of Brownian and Néel relaxation in magnetic fluids", J. Magn. Magn. Mater. **201**, 102 (1999).

[39] A. Labarta, O. Iglesias, Ll. Balcells and F. Badia, "Magnetic Relaxation in Small - Particle Systems: $\ln(t/\tau_0)$ Scaling", Phys. Rev. B, **48**, 10241 (1993).

[40] M. Rasa, "Magnetic Properties and Magneto - Birefringence of Magnetic Fluids", Eur. Phys. J. E **2**, 265 (2000).

[41] S. H. Kilcoyne and R. Cywinski, "Ferritin: A Model Superparamagnet", J. Magn. Magn. Mater. **140 - 144**, 1466 (1995).

[42] S. A. Makhlouf, F. T. Parker and A. E. Berkowitz, "Magnetic Hysteresis Anomalies in Ferritin", Phys. Rev. B **55**, R14717 (1997).

[43] S. A. Makhlouf, F. T. Parker, F. E. Spada, and A. E. Berkowitz, "Magnetic Anomalies in NiO Nanoparticles", J. Appl. Phys. **81**, 5561 (1997).

[44] M. S. Seehra, V. S. Babu, A. Manivannan and J. W. Lynn, "Neutron Scattering and Magnetic Studies of Ferrihydrite Nanoparticles", Phys. Rev. B **61**, 3513 (2000).

[45] M. S. Seehra and A. Punnoose, "Deviations from the Curie - Law Variation of Magnetic Susceptibility in Antiferromagnetic Nanoparticles", Phys. Rev. B **64**, 132410 (2001).

[46] A. Punnoose, T. Phanthavady, M. S. Seehra, N. Shah and G. P. Huffman, "Magnetic Properties of Ferrihydrite Nanoparticles Doped with Ni, Mo, and Ir", Phys. Rev. B **69**, 054425 (2004).

[47] N. J. O. Silva, V. S. Amaral, L. D. Carlos and V. D. Z. Bermudez, "Ferrihydrite Antiferromagnetic Nanoparticles in a Sol - Gel Derived Organic - Inorganic Matrix", J. Magn. Magn. Mater., **272 - 276**, 1549-1550 (2004).

[48] N. J. O. Silva, V. S. Amaral and L. D. Carlos, "Relevance of Magnetic Moment Distribution and Scaling Law Methods to Study the Magnetic Behavior of Antiferromagnetic Nanoparticles: Application to Ferritin", Phys. Rev. B **71**, 184408 (2005).

[49] S. Mørup and C. Frandsen, "Thermoinduced Magnetization in Nanoparticles of Antiferromagnetic Materials", Phys. Rev. Lett. **92**, 217201 (2004).

[50] N. J. O. Silva, V. S. Amaral, L. D. Carlos, B. R. González, L. M. Liz-Marzán, A. Millán, F. Palacio and V. D. Z. Bermudez, "Structural and magnetic studies in ferrihydrite nanoparticles formed within organic - inorganic hybrid matrices", J. Appl. Phys. **100**, 054301 (2006).

[51] S. D. Tiwari and K. P. Rajeev, "Effect of Distributed Particle Magnetic Moments on the Magnetization of NiO Nanoparticles", Solid State Communications **152**, 1080 (2012).

[52] C. Rani and S. D. Tiwari, "Estimation of Particle Magnetic Moment Distribution for Antiferromagnetic Ferrihydrite Nanoparticles", J. Magn. Magn. Mater. **385**, 272 (2015).

[53] C. Rani, S. D. Tiwari and D. Kumar, "Estimation of Particle Concentration in a Nanocomposite Using Magnetization Data", IEEE Transactions of Magnetics **51**, 6001005 (2015).

[54] D. A. Balaev et al., "Magnetic Properties and the Mechanism of Formation of the Uncompensated Magnetic Moment of Antiferromagnetic Ferrihydrite Nanoparticles of a Bacterial Origin", J. Exp. Theor. Phys. **119**, 479 (2014).

[55] C. Rani and S. D. Tiwari, "Superparamagnetic Behavior of Antiferromagnetic Six Lines Ferrihydrite Nanoparticles", Physica B **513**, 58 (2017).

[56] K. L. Pisane, E. C. Despeaux and M. S. Seehra, "Magnetic Relaxation and Correlating Effective Magnetic Moment with Particle Size Distribution in Maghemite Nanoparticles", J. Magn. Magn Mater. **384**, 148 (2015).

[57] K. L. Pisane, S. Singh and M. S. Seehra, "Synthesis, Structural Characterization and Magnetic Properties of Fe/Pt Core - Shell Nanoparticles", J. Appl. Phys. **117**, 17D708 (2015).

[58] D. E. Madsen, S. Mørup and M. F. Hansen, "On the Interpretation of Magnetization Data for Antiferromagnetic Nanoparticles", J. Magn. Magn. Mater. **305**, 95 (2006).

[59] M. Hanson, C. Johansson, M. S. Pedersen and S. Mørup, "The Influence of Particle Size and Interactions on the Magnetization and Susceptibility of Nanometre - Size Particles", J. Phys. Condens. Matter **7**, 9269 (1995).

[60] R. Fisker, J. M. Carstensen, M. F. Hansen, F. Bødker and S. Mørup, "Estimation of Nanoparticle Size Distributions by Image Analysis", J. Nanoparticle Res. **2**, 267 (2000).

[61] S. M. Gorun, G. C. Papaefthymiou, R. B. Frankel and S. J. Lippard, "Synthesis, Structure and Properties of an Undecairon (III) Oxo - Hydroxo Aggregate: An Approach to the Polyiron Core in Ferritin", J. Am. Chem. Soc. **109**, 3337 (1987).

[62] J. M. Cowley, D. E. Janney, R. C. Gerkin and P. R. Buseck, "The Structure of Ferritin Cores Determined by Electron Nanodiffraction", J. Struct. Biol. **131**, 210 (2000).

[63] P. M. Harrison, F. A. Fischbach, T. G. Hoy and G. H. Haggisi, "Ferric Oxyhydroxide Core of Ferritin", Nature **216**, 1188 (1967).

[64] K. M. Towe and W. F. Bradley, "Mineralogical Constitution of Colloidal "Hydrous Ferric Oxides" ", J. Colloid Interface Sci. **24**, 384 (1967).

[65] J. H. Jung, T. W. Eom, Y. P. Lee, J. Y. Rhee and E. H. Choi, "Magnetic Model for a Horse - Spleen Ferritin with a Three - Phase Core Structure", J. Magn. Magn. Mater. **323**, 3077 (2011).

[66] N. D. Chasteen and P. M. Harrison, "Mineralization in Ferritin: An Efficient Means of Iron Storage", J. Struct. Biol. **126**, 182 (1999).

[67] U. Schwertmann and R. M. Cornell, *Iron Oxides in the Laboratory: Preparation and Characterization* (Wiley - VCH, Germany, 2000).

[68] N. J. O. Silva, A. Millán, F. Palacio, E. Kampert, U. Zeitler, H. Rokato and V. S. Amaral, "Temperature Dependence of Antiferromagnetic Susceptibility in Ferritin", Phys. Rev. B **79**, 104405 (2009).

[69] N. J. O. Silva, V. S. Amaral, A. Urtizberea, R. Bustamante, A. Millán, F. Palacio, E. Kampert, U. Zeitler, S. de Brion, Ó. Iglesias and A. Labarta, "Shifted Loops and Coercivity from Field - Imprinted High - Energy Barriers in Ferritin and Ferrihydrite Nanoparticles", Phys. Rev. B **84**, 104427 (2011).

[70] D. A. Balaev et al., "Mechanism of the Formation of an Uncompensated Magnetic Moment in Bacterial Ferrihydrite Nanoparticles", J. Exp. Theor. Phys. Lett. **98**, 139 (2013).

[71] D. A. Balaev et al., "Change in the Magnetic Properties of Nanoferrihydrite with an Increase in the Volume of Nanoparticles During Low - Temperature Annealing", Phys. Solid State **58**, 1782 (2016).

[72] D. A. Balaev et al., "Magnetic Properties of Heat Treated Bacterial Ferrihydrite Nanoparticles", J. Magn. Magn. Mater. **410**, 171 (2016).

[73] C. Rani, "Effect of Particle Magnetic Moment Distribution on Magnetization of Antiferromagnetic Nanoparticle Systems", Ph. D. Thesis, Thapar Institute of Engineering & Technology, Patiala (2018).

[74] F. M. Michel, L. Ehm, S. M. Antao, P. L. Lee, P. J. Chupas, G. Liu, D. R. Strongin, M. A. A. Schoonen, B. L. Phillips and J. B. Parise, "The Structure of Ferrihydrite, A Nanocrystalline Material", Science **316**, 1726 (2007).

[75] F. Brem, G. Stamm and A. M. Hirt, "Modeling the Magnetic Behavior of Horse Spleen Ferritin with a Two - Phase Core Structure", J. Appl. Phys. **99**, 123906 (2006).

[76] N. Gálvez, B. Fernández, P. Sánchez, R. Cuesta, M. Ceolín, M. Clemente-León, S. Trasobares, M. López-Haro, J. J. Calvino, O. Stéphan and J. M. Domínguez-Vera, "Comparative Structural and Chemical Studies of Ferritin Cores with Gradual Removal of Their Iron Contents", J. Am. Chem. Soc. **130**, 8062 (2008).

[77] M. Preisinger, M. Krispin, T. Rudolf, S. Horn and D. R. Strongin, "Electronic Structure of Nanoscale Iron Oxide Particles Measured by Scanning Tunneling and Photoelectron Spectroscopies", Phys. Rev. B **71**, 165409 (2005).

[78] M. Krispin, A. Ullrich and S. Horn, "Crystal Structure of Iron - Oxide Nanoparticles Synthesized from Ferritin", J. Nanoparticle Research **14**, 669 (2012).

[79] J. T. Richardson and W. O. Milligan, "Magnetic Properties of Colloidal Nickelous Oxide", Phys. Rev. **102**, 1289 (1956).

[80] J. T. Richardson, D. I. Yiagas, B. Turk, K. Foster and M. V. Twigg, "Origin of Superparamagnetism in Nickel Oxide", J. Appl. Phys. **70**, 6977 (1991) .

[81] R. H. Kodama, S. A. Makhlouf and A. E. Berkowitz, "Finite Size Effects in Antiferromagnetic NiO Nanoparticles", Phys. Rev. Lett. **79**, 1393 (1997).

[82] S. D. Tiwari and K. P. Rajeev, "Signatures of Spin - Glass Freezing in NiO Nanoparticles", Phys. Rev. B **72**, 104433 (2005).

[83] S. D. Tiwari and K. P. Rajeev, "Paramagnetic to Ferromagnetic Transition and Superparamagnetic Blocking $Ni(OH)_2$ Nanoparticles", Phys. Rev. B **77**, 224430 (2008).

[84] D. A. Balaev et al., "Dynamic Magnetization Switching in NiO Nanoparticles: Pulsed Field Magnetometry Study", J. Supercond. Nov. Magn. **32**, 405 (2019).

[85] S. A. Makhlouf, H. Al-Attar and R. H. Kodama, "Particle Size and Temperature Dependence of Exchange Bias in NiO Nanoparticles", Solid State Commun. **145**, 1 (2008).

[86] B. D. Cullity, *Elements of X - Ray Diffraction* (Addison - Wesley Publishing Company, Inc., Reading, 1956).

[87] P. Gabbot, *Principle and applications of Thermal Analysis* (Blackwell Publishing Ltd., UK, 2008).

[88] D. B. Williams and C. B. Carter, *Transmission Electron Microscopy - A Textbook for Materials Science* (Springer, New York, 1996).

[89] Jon C. Van Lon, *Analytical Atomic Absorption Spectroscopy* (Academic Press, Inc., USA, 1980).

[90] S. Foner, "Versatile and Sensitive Vibrating - Sample Magnetometer", Rev. Sci. Instrum. **30**, 548 (1959).

[91] S. Davis, in *Colloid Science Principles, Methods and Applications* edited by T. Cosgrove (John Wiley and Sons Ltd., United Kingdom, 2010), p. 317.

[92] I. M. Weiss, C. Muth, R. Drumm and H. O. K. Kirchner, "Thermal Decomposition of the Amino Acids Glycine, Cysteine, Aspartic Acid, Asparagine, Glutamic Acid, Glutamine, Arginine and Histidine", BMC Biophysics **11**, 2 (2018).

[93] C. Rani and S. D. Tiwari, "Phase Transitions in Two - Line Ferrihydrite Nanoparticles", Appl. Phys. A **123**, 532 (2017).

[94] V. de la Fuente et al., "Plant Tissues and Embryos Biominerals in Sarcocornia Pruinosa, a Halophyte from the Río Tinto Salt Marshes", Minerals **8**, 505 (2018).

[95] M. Darbandi et al., "Nanoscale Size Effect on Surface Spin Canting in Iron Oxide Nanoparticles Synthesized by the Microemulsion Method", J. Phys. D: Appl. Phys. **45**, 195001 (2012).

[96] T. Swain and G. S. Brahma, "Synthesis, Characterization, and Thermal Behavior of $Ni_3(PO_4)_2{\cdot}8H_2O{\cdot}Na_3PO_4{\cdot}3.5H_2O{\cdot}0.75Na_2SO_4$", J. Elect. Mater. **47**, 2817 (2018).

[97] M. Mobin, "High Temperature Interactions of Metal Oxides and Carbides with Ionic Salts", Sci. Eng. Compos. Mater. **8**, 257 (1999).

[98] M. Mobin, A. U. Malik and S. Ahmad, "High Temperature Interactions of Metal Oxides With NaCl", J. Less Common Metals **160**, 1 (1990).

[99] M. Broström, S. Enestam, R. Backman and K. Mäkelä, "Condensation in the KCl - NaCl System", Fuel Processing Technology **105**, 142 (2013).

[100] S. Zhou, Y. Wei, B. Li, H. Wang, B. Ma and C. Wang, "Mechanism of Sodium Chloride in Promoting Reduction of High Magnesium Low - Nickel Oxide Ore", Sci. Rep. **6:29061**,1 (2016).

[101] T. A. Rafter, "Sodium Peroxide Decomposition of Minerals in Platinum Vessels", Analyst **75**, 485 (1950).

[102] Y. Goto, "The Effect of Squeezing on the Phase Transformation and Magnetic Properties of γ - Fe_2O_3", Jpn. J. Appl. Phys. **3**, 739 (1964).

[103] P. Ayyub, M. Multani, M. Barma, V. R. Palkar and R. Vijayaraghavan, "Size - Induced Structural Phase Transitions and Hyperfine Properties of Microcrystalline Fe_2O_3", J. Phys. C: Solid State Phys. **21**, 2229 (1988).

[104] Y. El Mendili, J. F. Bardeau, N. Randrianantoandro, J. M. Greneche and F. Grasset, "Structural Behavior of Laser - Irradiated γ - Fe_2O_3 Nanocrystals Dispersed in Porous Silica Matrix: γ - Fe_2O_3 to α - Fe_2O_3 Phase Transition and Formation of ϵ - Fe_2O_3", Sci. Technol. Adv. Mater. **17**, 597 (2016).

[105] G. Gnanaprakash, S. Ayyappan, T. Jayakumar, J. Philip and B. Raj, "Magnetic Nanoparticles with Enhanced γ - Fe_2O_3 to α - Fe_2O_3 Phase Transition Temperature", Nanotechnology **17**, 5851 (2006).

[106] M. S. Seehra, V. Singh, X. Song, S. Bali and E. M. Eyring, "Synthesis, Structure and Magnetic Properties of Non - Crystalline Ferrihydrite Nanoflakes", J. Phys. Chem. Solids **71**, 1362 (2010).

[107] M. M. Ibrahim, J. Zhao and M. S. Seehra, "Determination of Particle Size Distribution in an Fe_2O_3 Based Catalyst Using Magnetometry and X -ray Diffraction", J. Mater. Res. **7**, 1856 (1992).

[108] F. Reif, *Fundamentals of Statistical and Thermal Physics* (McGraw Hill, Singapore, 1985), p. 212.

[109] J. Ma and K. Chen, "Discovery of Superparamagnetism in Sub - Millimeter - Sized Magnetite Porous Single Crystals", Phys. Lett. A **380**, 3313 (2016).

[110] K. Kurosawa, M. Miura and S. Saito, "Magnetic Torque Measurements on NiO (111) Platelets", J. Phys. C: Solid State Phys. **13**,1521 (1980).

[111] S. Saito, M. Miura and K. Kurosawa, "Optical Observations of Antiferromagnetic S Domains in NiO (111) Platelets", J. Phys. C: Solid State Phys. **13**, 1513 (1980).

[112] K. L. Pisane, S. Singh and M. S. Seehra, "Unusual Enhancement of Effective Magnetic Anisotropy with Decreasing Particle Size in Maghemite Nanoparticles", Appl. Phys. Lett. **110**, 222409 (2017).

[113] C. R. H. Bahl, K. Lefmann, L. T. Kuhn, N. B. Christensen, H. Vázquez and S. Mørup, "Spin Dynamics in Weakly and Strongly Interacting NiO Nanoparticles", J. Phys.: Condens. Matter **18**, 11203 (2006).